



An improved theory of the response of DIII-D H-mode discharges to static resonant magnetic perturbations and its implications for the suppression of edge localized modes



Cite as: Phys. Plasmas **27**, 072501 (2020); <https://doi.org/10.1063/5.0011738>
 Submitted: 23 April 2020 . Accepted: 05 June 2020 . Published Online: 01 July 2020

R. Fitzpatrick , and A. O. Nelson 

COLLECTIONS



This paper was selected as Featured



View Online



Export Citation



CrossMark

ARTICLES YOU MAY BE INTERESTED IN

[Role of sheared \$E \times B\$ flow in self-organized, improved confinement states in magnetized plasmas](#)

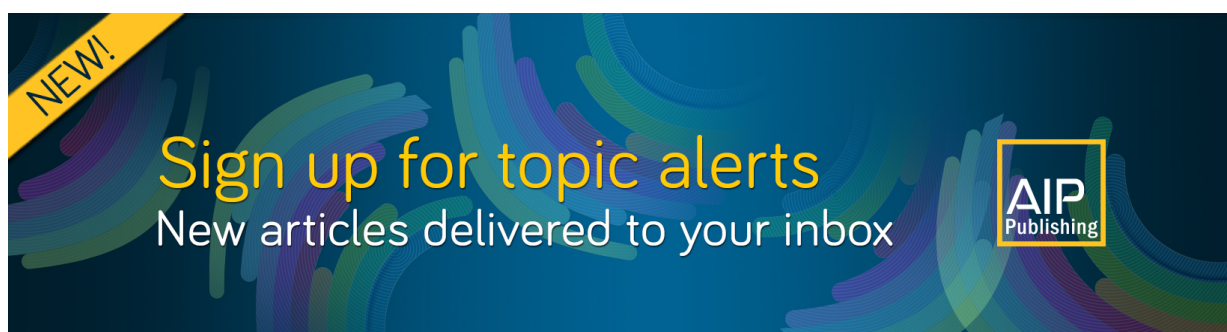
Physics of Plasmas **27**, 060501 (2020); <https://doi.org/10.1063/1.5142734>

[A new explanation of the sawtooth phenomena in tokamaks](#)

Physics of Plasmas **27**, 032509 (2020); <https://doi.org/10.1063/1.5140968>

[Theory of edge localized mode suppression by static resonant magnetic perturbations in the DIII-D tokamak](#)

Physics of Plasmas **27**, 042506 (2020); <https://doi.org/10.1063/5.0003117>



An improved theory of the response of DIII-D H-mode discharges to static resonant magnetic perturbations and its implications for the suppression of edge localized modes

Cite as: Phys. Plasmas **27**, 072501 (2020); doi: [10.1063/5.0011738](https://doi.org/10.1063/5.0011738)

Submitted: 23 April 2020 · Accepted: 5 June 2020 ·

Published Online: 1 July 2020



View Online



Export Citation



CrossMark

R. Fitzpatrick^{1,a)}  and A. O. Nelson² 

AFFILIATIONS

¹Institute for Fusion Studies, Department of Physics, University of Texas at Austin, Austin, Texas 78712, USA

²Princeton Plasma Physics Laboratory, Princeton, New Jersey 08543, USA

^{a)}Author to whom correspondence should be addressed: rfitzp@farside.ph.utexas.edu

ABSTRACT

The plasma response to an externally generated, static, $n = 2$, resonant magnetic perturbation (RMP) in the pedestal region of DIII-D H-mode discharge #158115 is investigated using a toroidal generalization of the asymptotic matching model presented by Fitzpatrick [Phys. Plasmas **27**, 042506 (2020)]. Just as in a recent paper [Q. M. Hu *et al.*, Phys. Plasmas **26**, 120702 (2019)], it is hypothesized that the density pump-out phenomenon is due to locked magnetic island chains induced at the bottom of the pedestal, whereas the suppression of edge localized modes is associated with a locked magnetic island chain induced at the top of the pedestal. Neutral penetration inside the last closed magnetic flux-surface is found to have a significant influence on locked magnetic island chain formation at the bottom of the pedestal. It is found that locked island formation at the top of the pedestal is only possible when q_{95} lies in certain narrow windows. Finally, it is inferred that, in order to successfully induce a locked island chain at the top of the pedestal, an external RMP field-coil system must generate a magnetic field that is simultaneously strongly amplified by the plasma (via the ideal kink response) and has a large resonant component at a rational surface that lies close to the top of the pedestal.

Published under license by AIP Publishing. <https://doi.org/10.1063/5.0011738>

I. INTRODUCTION

Tokamak discharges operating in high-confinement mode (H-mode)¹ exhibit intermittent bursts of heat and particle transport, emanating from the outer regions of the plasma that are known as “type-I edge localized modes” (ELMs).² Large ELMs can cause a problematic influx of tungsten ions into the plasma core in present-day tokamaks possessing tungsten plasma-facing components.³ Moreover, it is estimated that the heat load that ELMs will deliver to the tungsten plasma-facing components in a reactor-scale tokamak, such as ITER, will be large enough to cause massive tungsten ion influx into the plasma core and that the erosion associated with this process will unacceptably limit the lifetimes of these components.⁴ Consequently, the development of robust and effective methods for ELM control is a high priority for the international magnetic fusion program.

The most promising method for the control of ELMs in H-mode tokamak discharges is via the application of static “resonant magnetic perturbations” (RMPs). Complete RMP-induced ELM suppression

was first demonstrated on the DIII-D tokamak.⁵ Subsequently, either mitigation or complete suppression of ELMs has been demonstrated on the JET,⁶ ASDEX-U,⁷ KSTAR,⁸ MAST,⁹ and EAST¹⁰ tokamaks.

ELMs are thought to be caused by peeling-ballooning instabilities, with intermediate toroidal mode numbers, that are driven by the strong pressure and current density gradients characteristic of the edge region of an H-mode tokamak discharge,¹¹ which is generally known as the “pedestal” region.

The initial observations of RMP-induced ELM suppression were interpreted as an indication that the magnetic field in the pedestal is rendered completely stochastic by the applied RMP, leading to greatly enhanced transport via thermal diffusion along magnetic field-lines.^{5,12} This explanation was quickly abandoned because no significant reduction in the electron temperature gradient in the pedestal is observed during RMP-induced ELM suppression experiments, whereas a very significant reduction would be expected in the presence of completely stochastic fields. It is now generally accepted that response currents

generated within the pedestal, as a consequence of plasma flow, play a crucial role in the perturbed equilibrium in the presence of RMPs, and that these currents act to prevent the formation of RMP-driven magnetic island chains—a process known as “shielding”—and, thereby, significantly reduce the stochasticity of the magnetic field.¹³

The application of a static RMP, resonant in the pedestal region, to an H-mode tokamak discharge is observed to give rise to two distinct phenomena.^{14–18} The first of these is the so-called “density pump-out,” which is characterized by a reduction in the electron number density in the pedestal region that varies smoothly with the amplitude of the applied RMP, is accompanied by a similar, but significantly smaller, reduction in the electron and ion temperatures, but is not associated with ELM suppression. The second phenomenon is “ELM suppression,” which occurs when the amplitude of the applied RMP exceeds a certain threshold value, and is accompanied by sudden changes in the electron number density profile, the electron and ion temperature profiles, and the ion toroidal angular velocity profile, in the pedestal region. ELM suppression is only observed to take place when q_{95} (i.e., the safety-factor on the magnetic flux-surface that encloses 95% of the poloidal flux enclosed by the last closed flux-surface) takes values that lie in certain narrow windows.^{17,18}

Recent numerical simulations [made using the cylindrical, nonlinear, two-fluid, reduced-magnetohydrodynamical (MHD), initial-value code, TM1^{19–21}] have shed considerable light on the hitherto poorly understood physical mechanism that underlies RMP-induced ELM suppression in H-mode tokamak discharges.²² The simulations in question make a plausible case that the density pump-out phenomenon is associated with the formation of locked magnetic island chains at the bottom of the pedestal, whereas the ELM suppression phenomenon is associated with the formation of a locked magnetic island chain at the top of the pedestal.

Nonlinear extended-MHD simulations of the response of a tokamak plasma to an RMP are extremely time consuming, especially when performed in full toroidal geometry.²³ There are two main reasons for this inefficiency. The first reason is the presence of widely disparate timescales in the problem. For instance, the ratio of the resistive diffusion timescale to the Alfvén timescale, which is known as the Lundquist number, is typically 10^8 in the pedestals of modern-day tokamak plasmas and is likely to rise to 10^{10} in the ITER pedestal. If the code in question is explicit, then it is limited to taking very small (i.e., sub-Alfvénic) time-steps in order to avoid numerical instabilities. This is problematic because, to be useful, the simulation needs to be run for at least one resistive diffusion timescale. On the other hand, if the code is implicit then each time step involves the numerically intensive inversion of an extremely ill-conditioned matrix (whose condition number is of order the Lundquist number). The second reason for the inefficiency of extended-MHD codes is the development of thin current sheets at various resonant surfaces in the plasma, which necessitates very fine resolution in the radial direction. The current sheets become thinner as the Lundquist number of the plasma increases.

An alternative, and much more efficient, approach to the direct numerical simulation of the response of a tokamak plasma to an applied RMP involves the application of “asymptotic matching” theory. According to standard asymptotic matching theory, the response of the plasma to the applied RMP is governed by the relatively simple equations of linear, marginally stable (i.e., $\partial/\partial t \equiv 0$), “ideal” MHD, to an excellent approximation, everywhere in the plasma, apart from a

number of relatively narrow (in the radial direction) regions in which the applied perturbation resonates with the equilibrium magnetic field.^{24–29} Magnetic reconnection can take place within the resonant regions to produce relatively thin nonlinear magnetic island chains. The splitting of the problem into two parts in asymptotic matching theory depends on the fact that the resistive term in the plasma Ohm’s law is generally many orders of magnitude smaller than the other terms. Moreover, the scalar pressure gradient and the $\mathbf{j} \times \mathbf{B}$ terms in the plasma equation of motion are generally many orders of magnitude larger than the inertial, neoclassical viscous, or perpendicular viscous terms. However, the small terms become significant in the immediate vicinities of the various resonant regions because the radial scale length there becomes of order a nonlinear magnetic island width, which is generally much less than the plasma minor radius. Thus, when employing the asymptotic matching approach, the equations of linear, marginally stable, ideal-MHD are solved in the so-called “outer region” that comprises most of the plasma (and the surrounding vacuum), the time-varying equations of nonlinear extended-MHD are solved in the various resonant layers that constitute the so-called “inner region,” and the two sets of solutions are then asymptotically matched to one another. The main advantage of asymptotic matching theory is that it actually becomes more accurate as the disparity between the various timescales and lengthscales in the problem increases.

Asymptotic matching theory was used in Ref. 30 to investigate the response of a typical DIII-D H-mode tokamak plasma to an applied RMP, resonant in the pedestal region, for the simple case in which the plasma equilibrium is approximated as a periodic cylinder. The results obtained in this paper were broadly similar to those reported in Ref. 22. The aim of the present paper is to extend the theory developed in Ref. 30 to take into account the toroidal nature of a realistic tokamak plasma equilibrium.

II. DESCRIPTION OF THE MODEL

A. Introduction

The model employed in this paper is presented in its entirety in [Appendixes A–E](#). The aim of this section is to outline the salient features of the model.

B. Electromagnetic plasma response

The theory used to describe the electromagnetic response of a toroidal tokamak equilibrium to an externally applied RMP is presented in [Appendix A](#). It should be noted that a toroidal tokamak equilibrium exhibits two distinct types of response to an applied RMP.^{18,31,32} The first of these is known as the “tearing response”—this is a non-ideal-MHD response that is associated with the formation of current sheets and magnetic island chains at various resonant surfaces within the plasma. The second response type is known as the “kink response”—this is an edge-localized ideal-MHD response that is associated with coupling to a stable non-resonant kink mode. The kink response is also associated with the amplification of the applied RMP by the plasma.

For the case of the tearing response, it is argued in [Appendix A](#) that, because resonant surfaces in the pedestal region of an H-mode tokamak plasma inevitably resonate with helical harmonics of the applied RMP possessing poloidal mode numbers that are much greater than unity, it is a good approximation to treat the plasma response as

vacuum-like (i.e., $\delta\mathbf{J} = \mathbf{0}$) between the various resonant surfaces. In this limit, radially thin current sheets form at the resonant surfaces. Moreover, these sheets consist of current filaments that run parallel to the local equilibrium magnetic field. The electromagnetic interaction between the various current sheets in the plasma can be calculated from the Biot-Savart law. The result is a toroidal tearing mode dispersion relation of the form [see Eq. (A56)]

$$\Psi_k = \sum_{k'=1,K} F_{kk'} \Delta\Psi_k \quad (1)$$

for $k = 1, K$. Here, k and k' index the K (say) resonant surfaces in the plasma. Moreover, Ψ_k and $\Delta\Psi_k$ parameterize the reconnected magnetic flux and the current sheet strength, respectively, at the k th surface. The off diagonal elements of the dimensionless Hermitian matrix $F_{kk'}$ are the normalized mutual inductances between the various current sheets, whereas the diagonal elements are the normalized self-inductances of the current sheets. In the presence of non-axisymmetric currents flowing in external poloidal magnetic field coils, the previous dispersion relation generalizes to give [see Eq. (A68)]

$$\Delta\Psi_k = \sum_{k'=1,K} E_{kk'} \Psi_{k'} + |E_{kk}| \chi_k, \quad (2)$$

where $E_{kk'}$ is the inverse of the $F_{kk'}$ matrix. The quantity χ_k that appears in the previous equation is the reconnected magnetic flux driven at the k th resonant surface by the external currents when there is no shielding of driven magnetic reconnection at the surface in question (i.e., $\Delta\Psi_k = 0$), but perfect shielding at all of the other resonant surfaces (i.e., $\Psi_{k' \neq k} = 0$). The real quantity E_{kk} represents the standard tearing stability index²⁴ (normalized to the minor radius of the resonant surface) for a tearing mode that only reconnects magnetic flux at the k th resonant surface.²⁵ Given that there are no sources of plasma free energy in our tearing response model, we expect all of the E_{kk} to be negative. In other words, we expect the plasma to be tearing stable.

For the case of the kink response of the plasma to the applied RMP, we introduce a heuristic control surface, labeled $K+1$, located on the plasma boundary (see Appendix A 8). This surface is presumed to act like a resonant surface whose poloidal mode number is $m_{K+1} = m_K + 1$ (where m_K is the poloidal mode number of the outermost resonant surface in the plasma). The quantity $E_{K+1,K+1}$ is replaced by $-s_{\text{kink}}$, where s_{kink} is a dimensionless adjustable parameter. We expect there to be no shielding current at the control surface (i.e., $\Delta\Psi_{K+1} = 0$). The net result is a modified version of Eq. (2) in which the χ_k values are amplified by the plasma. We interpret this amplification as being due to coupling to a stable non-resonant kink mode. The stability of the kink mode is governed by the parameter s_{kink} . The mode is extremely stable in the limit $s_{\text{kink}} \rightarrow \infty$ (in which case there is no amplification) and approaches marginal stability as $s_{\text{kink}} \rightarrow 0$ (in which case the amplification becomes very strong).

In principle, as is described in Appendix A 8, the correct χ_k values, which epitomize the kink response of the plasma to the applied RMP, can be calculated by the GPEC code.³³ In future, this is how the χ_k values will be determined.

C. Neoclassical physics

The purpose of the neoclassical calculation described in Appendix B is to determine the values of six quantities needed by the

overall model. (Here, we are assuming that there is a single ion impurity species. However, the generalization to multiple impurity species is straightforward. The requisite number of neoclassical parameters is four plus two times the number of impurity species.) The first of these quantities is the dimensionless majority-ion neoclassical viscosity, μ_{00}^i ; this quantity is used to determine the neoclassical poloidal flow damping timescale [see Eq. (C7)]. The second quantity is the dimensionless electron neoclassical viscosity Q_{00}^e ; this quantity is used to determine the neoclassical and plasma impurity modifications to the plasma electrical conductivity [see Eq. (D4)]. The final four quantities are denoted as L_{00}^{ii} , L_{01}^{ii} , L_{00}^{ii} , and L_{01}^{ii} ; these dimensionless quantities describe how the neoclassical viscosities of the majority and impurity ions, as well as charge exchange with neutrals, determine the intrinsic neoclassical poloidal angular velocity of the majority ions. The intrinsic poloidal angular velocity of the majority ions is important because it governs the so-called “natural frequency” of a nonlinear magnetic island chain at a given resonant surface [see Eq. (D9)]. The natural frequency of an island chain is the helical phase velocity it would have were it naturally unstable.³⁴

The neoclassical theory described in Appendix B is more accurate and self-consistent than that presented in Ref. 30. In the latter case, Q_{00}^e is calculated from the well-known model of Sauter *et al.*³⁵ whereas the other neoclassical parameters are calculated from the equally well-known model of Kim *et al.*^{36,37} In the present paper, all neoclassical coefficients are calculated using the more general analysis of Hirshman and Sigmar.³⁸ Unlike the neoclassical theory used in Ref. 30, in this paper, we do not assume that the impurity ion mass is much larger than the majority ion mass or that the impurity ion viscous force is negligible with respect to the friction force between the impurity and majority ion species. We also calculate the fraction of trapped particles and the transit frequencies exactly, rather than relying on analytical approximations. Moreover, the interpolation between the three neoclassical collisionality regimes is performed in the most accurate possible manner (by employing a Padé approximation prior to the final velocity-space integral). Finally, the charge state of the impurity ions is calculated self-consistently as a function of the plasma density and temperature using data obtained from the FLYCHK code.³⁹

The incorporation of charge exchange with neutrals represents a particularly important improvement to the neoclassical calculation. It is well known that friction with neutrals, due to charge exchange reactions in the scrape-off layer, is responsible for fixing the edge rotation of a tokamak plasma.³⁴ Without this friction, the edge rotation (and, hence, the internal rotation) would be free to change its value, which would imply that even the smallest externally generated electromagnetic torque exerted at a resonant surface within the plasma would be capable of modifying the local plasma rotation so as to produce mode penetration. In other words, there would be no shielding of driven magnetic reconnection at resonant surfaces due to plasma flow in the absence of the neutral friction. However, it is well known that neutrals penetrate a small distance inside the last closed magnetic flux surface (LCFS) and that charge exchange reactions between these neutrals and the majority ions can significantly change the prediction for the intrinsic neoclassical poloidal velocity of the majority ions just inside the LCFS.^{40,41} Given that we are interested in the response of an H-mode tokamak plasma to an RMP that possesses resonant surfaces close to the edge of the plasma and that the intrinsic neoclassical poloidal

rotation plays an important role in determining this response, it is clearly important to incorporate neutral penetration into our model.

D. Plasma angular velocity evolution

Appendix C describes how the evolution of the plasma poloidal and toroidal angular velocity profiles is determined. The analysis depends on the fact that, in a high Lundquist number plasma with subsonic levels of plasma flow, the flux-surface averaged poloidal and toroidal electromagnetic torques are negligible, except in the immediate vicinities of the various resonant surfaces within the plasma.³⁴ Moreover, it is an excellent approximation to neglect the finite radial thicknesses of the regions in the vicinities of the various resonant surfaces in which the torque is non-negligible. It is convenient to represent the poloidal and toroidal angular velocity profiles as weighted sums of appropriate Bessel functions. In this manner, the evolution of the plasma poloidal and toroidal angular velocity profiles reduces to the solutions of a set of coupled first-order ordinary differential equations. The plasma angular velocity evolution model described in Appendix C is identical to that used in Ref. 30, except that we now allow electromagnetic torques to develop at multiple resonant surfaces in the plasma, rather than at a single resonant surface.

E. Electromagnetic response in inner region

Appendix D describes how the electromagnetic response of the plasma to the externally applied RMP is determined in the immediate vicinities of the various resonant surfaces. The response is governed by “nonlinear” magnetic island physics.³⁰ This is the case because, in a high temperature tokamak plasma, flow shielding is not sufficiently strong to reduce the widths of the magnetic island chains that develop at the resonant surfaces below the associated linear layer widths (which is a necessary criterion for the validity of linear response theory).³⁰ The nonlinear response model at a given resonant surface consists of an island width evolution equation, combined with a no-slip constraint that relates the island helical phase velocity to the local plasma flow. The resonant response model described in Appendix D is identical to that used in Ref. 30, except that we now allow magnetic island chains to develop at multiple resonant surfaces in the plasma, rather than at a single resonant surface.

F. Complete model

The complete model is summarized in Appendix E. The model consists of a large number of coupled first-order ordinary differential equations that must be evolved in time. According to these equations, the magnetic island chains induced by the RMP at the various resonant surfaces in the plasma are coupled together electromagnetically (via the off diagonal elements of the $E_{kk'}$ matrix) but are also coupled together via modifications that island-induced electromagnetic torques make to the plasma poloidal and toroidal angular velocity profiles.

III. EXAMPLE CALCULATION

A. Introduction

In this paper, we make use of a series of model toroidal plasma equilibria derived from the experimental plasma equilibrium in DIII-D H-mode discharge #158115 at time $t = 3250$ ms (at which time, the components of the RMP that are resonant within the plasma are too small to cause significant density pump-out or mode penetration).¹⁷

The experimental equilibrium has been modified by the ISOLVER code⁴² in such a manner that the safety-factor profile [see Eq. (A3)] is rescaled as follows:

$$q(\Psi_N) \rightarrow q(0) + [q_{95} - q(0)] \left[\frac{q(\Psi_N) - q(0)}{q(0.95) - q(0)} \right], \quad (3)$$

where q_{95} is the target safety-factor value at the 95% normalized magnetic flux surface (i.e., $\Psi_N = 0.95$), and $q(0) = 1.026$ and $q(0.95) = 4.38$ are the original safety-factor values at the magnetic axis and the 95% normalized magnetic flux surface, respectively. (Here, the normalized equilibrium poloidal magnetic flux, Ψ_N , is defined in Appendix A.2.) The pressure profile and the boundary shape are not modified by ISOLVER. The result is a family of self-similar equilibria with the same boundary shapes, pressure profiles, and central safety-factors, but different q_{95} values.

B. Plasma equilibrium

Figure 1 shows contours of $\Psi_N(R, Z)$ (see Appendix A.1) for an example plasma equilibrium with $q_{95} = 4.58$. The scale major radius and toroidal magnetic field strength (see Appendix A.1) take the values $R_0 = 1.66$ m and $B_0 = 1.74$ T, respectively. The locations of the sections of the I-coil,⁴³ which generates the RMP, are indicated in the figure. In this paper, as is the case in DIII-D discharge #158115, the I-coil is used to produce an RMP with $n = 2$ periods in the toroidal direction. Note that the experimental g-file has been run through the CHEASE code⁴⁴ in order to soften the X-point structure. (Hence, the Ψ_N values outside the plasma boundary are fictitious.) This procedure only modifies the equilibrium at the very edge of the plasma (i.e., $\Psi_N > 0.995$) and is necessary for numerical convenience. We intend to improve this aspect of the calculation in the future.

Figures 2 and 3 show the safety-factor, total pressure, electron number density, electron temperature, and $\mathbf{E} \times \mathbf{B}$ frequency [see Eq. (15)] profiles in our example equilibrium. All of these profiles are derived from experimental data,¹⁷ except that the safety-factor profile has been rescaled according to Eq. (3). It can be seen that there are 11 resonant surfaces in the plasma (i.e., $K = 11$).

The analysis in this paper makes use of a magnetic flux-surface label, r (see Appendix A.1), that has the dimensions of length. The relationship between this label and the normalized equilibrium poloidal magnetic flux for our example equilibrium is shown in Fig. 4. Note that $r = 0$ on the magnetic axis, and $r = a$ on the plasma boundary, where $a = 0.855$ m.

C. Resonant magnetic perturbation

In this paper, the resonant magnetic perturbation is generated by running currents that modulate as $e^{-in\phi}$, where $n = 2$ and ϕ is the geometric toroidal angle (see Appendix A.1), through the toroidal sections of the I-coil shown in Fig. 1. Let $\Delta\phi_{UL}$ be the phase difference between the currents run through the upper and lower sections of the I-coil. The amplitude of the resonant component of the RMP at the k th resonant surface is measured by the parameter $|\chi_k|$ [see Eq. (2)]. Figure 5 shows $\tilde{\chi}_k = |\chi_k|/(R_0 B_0)$, for $k = 1, K$, calculated as a function of $\Delta\phi_{UL}$ for our example plasma equilibrium when 1 kA flows through the I-coil. Two cases are shown. In the first case, $s_{\text{kink}} = \infty$, which implies that there is no amplification of the RMP due to the kink response of the plasma. In the second case, $s_{\text{kink}} = 2$, which implies

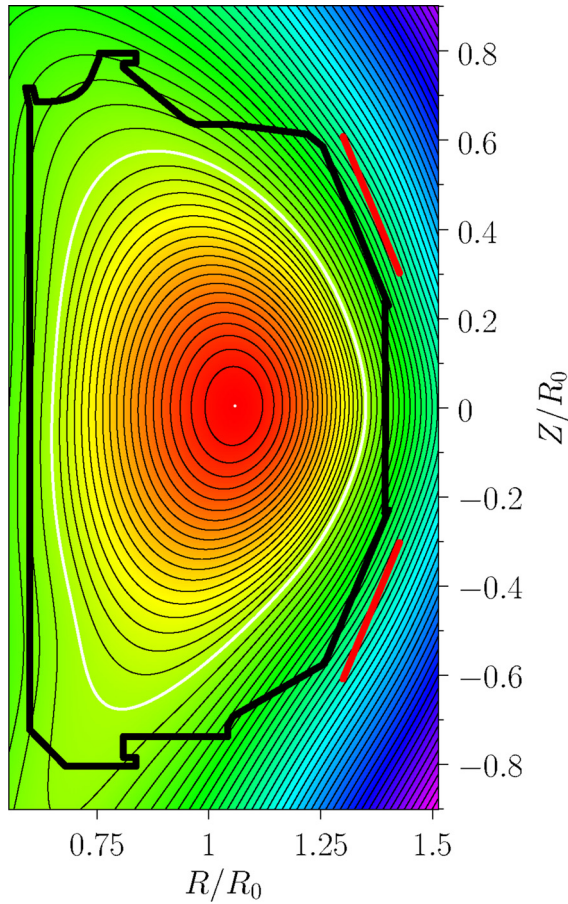


FIG. 1. Contours of $\Psi_N(R, Z)$ for a model DIII-D plasma equilibrium with $q_{95} = 4.58$. The white contour shows the location of the LCFS. The heavy black curve shows the location of the limiter. The red lines show the location of the upper and lower sections of the I-coil.

that the RMP is amplified by the plasma to some extent. A comparison of the two cases reveals that the plasma preferentially amplifies those helical harmonics of the RMP that resonate close to the edge of the plasma. This is not surprising, because the stable kink mode that is responsible for the amplification is resonant just outside the plasma boundary.

D. Natural frequencies

The natural frequency of an RMP-induced magnetic island chain is the helical frequency with which it would propagate (in the absence of the RMP) were it naturally unstable.³⁴ This quantity plays a key role in mode penetration theory because mode penetration (i.e., locked island formation) at a given resonant surface becomes particularly easy when the associated natural frequency approaches zero.³⁴ The natural frequency of a nonlinear magnetic island chain is largely determined by neoclassical physics (via the neoclassical stress tensor).⁴⁵

In the neoclassical calculations performed in this paper, the majority and minority ions are assumed to be deuterium (i.e., $m_i = 2$) and carbon (i.e., $m_i = 12.001$), respectively, as is indeed the case in

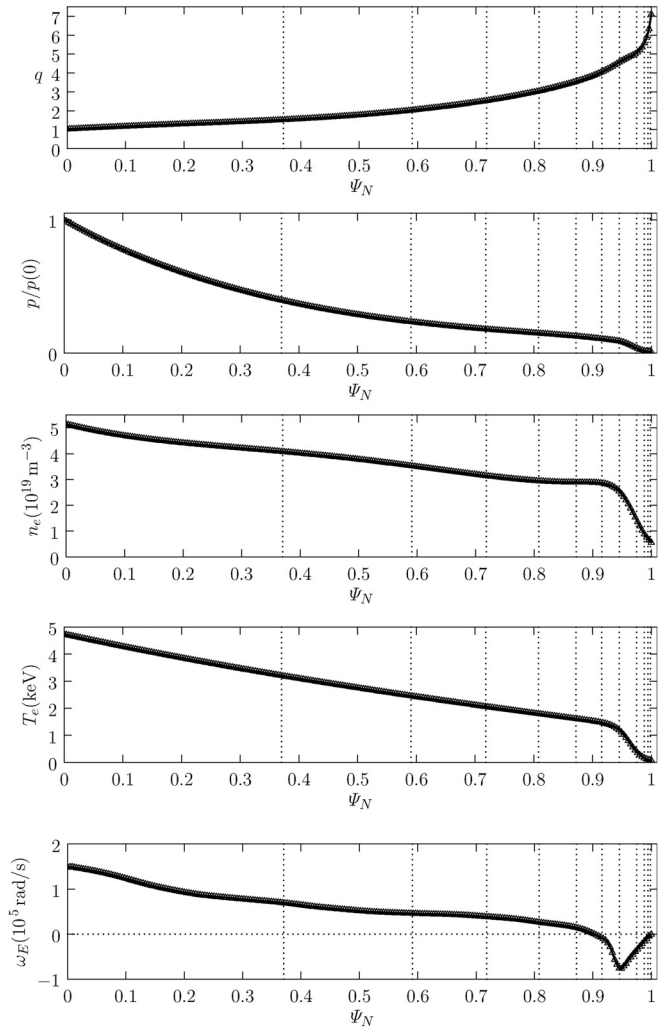


FIG. 2. The safety-factor, total pressure, electron number density, electron temperature, and $\mathbf{E} \times \mathbf{B}$ frequency profiles for a model DIII-D plasma equilibrium with $q_{95} = 4.58$. The vertical lines show the locations of the $m = 3/n = 2, 4/2, 5/2, 6/2, 7/2, 8/2, 9/2, 10/2, 11/2, 12/2$, and $13/2$ resonant surfaces, in order from the left to the right. Here, $p(0) = 1.23 \times 10^6$ Pa.

DIII-D discharge #158115. The effective ion charge number, Z_{eff} , is assumed to take the constant value 2.5 throughout the pedestal. This assumption is in accordance with line emission spectroscopy data. The electron, majority ion, and impurity ion temperatures are all assumed to be equal in the pedestal. This is a reasonably accurate assumption in DIII-D H-mode discharges. The neutral atoms that penetrate inside the LCFS and into the pedestal are assumed to be deuterium atoms. The flux-surface averaged neutral deuterium atom number density takes the form (see Appendix B 6)

$$\langle n_n \rangle(r) = \langle n_n \rangle(a) \exp\left(\frac{r-a}{l_n}\right), \quad (4)$$

where $\langle n_n \rangle(a) = 3 \times 10^{17} \text{ m}^{-3}$ and $l_n = 1.2 \times 10^{-2} \text{ m}$.⁴¹ The flux-surface neutral poloidal asymmetry parameter

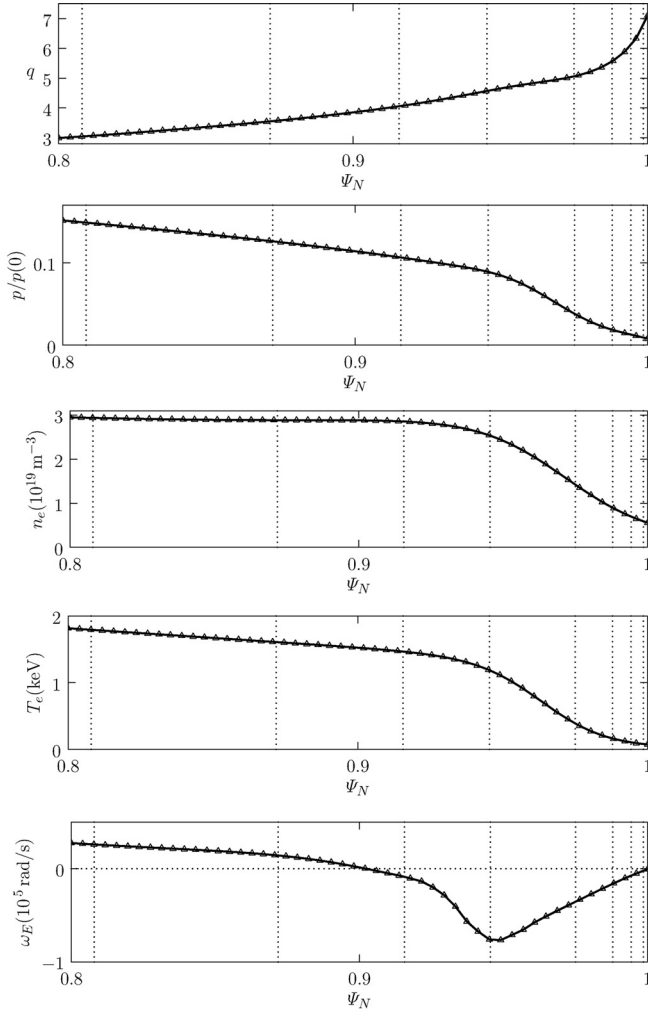


FIG. 3. The safety-factor, total pressure, electron number density, electron temperature, and $\mathbf{E} \times \mathbf{B}$ frequency profiles in the pedestal of a model DIII-D plasma equilibrium with $q_{95} = 4.58$. The vertical lines show the locations of the $m = 6/n = 2, 7/2, 8/2, 9/2, 10/2, 11/2, 12/2$, and $13/2$ resonant surfaces, in order from the left to the right. Here, $p(0) = 1.23 \times 10^6$ Pa.

$$\gamma_n = \frac{\langle n_n \rangle \langle B^2 \rangle}{\langle n_n B^2 \rangle} \quad (5)$$

is given the value 1.5.⁴¹ The flux-surfaced averaged deuterium-atom/deuterium-ion charge exchange rate constant is⁴⁶

$$\langle \sigma v \rangle_i^{cx} = 4 \times 10^{-14} \text{ m}^3 \text{ s}^{-1}. \quad (6)$$

The neutrals are assumed to be cold (i.e., $E_n/T_i = 0$). However, the opposite assumption that the neutrals are hot (i.e., $E_n/T_i = 1$) does not appreciably modify the results of the calculation. Finally, the value of C in Eq. (B14) is 10.

Figure 6 shows the natural frequencies calculated at resonant surfaces located in the pedestal of our example plasma equilibrium. For comparison, the natural frequencies predicted by linear theory (which implies that magnetic island chains are convected by the local electron

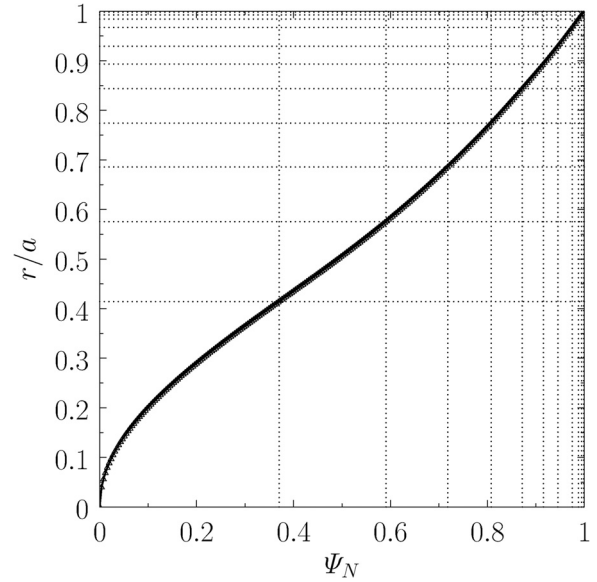


FIG. 4. Relationship between the flux-surface label r and the normalized equilibrium poloidal magnetic flux, Ψ_N , for a model DIII-D plasma equilibrium with $q_{95} = 4.58$. The horizontal and vertical lines indicate the locations of the $n=2$ resonant surfaces.

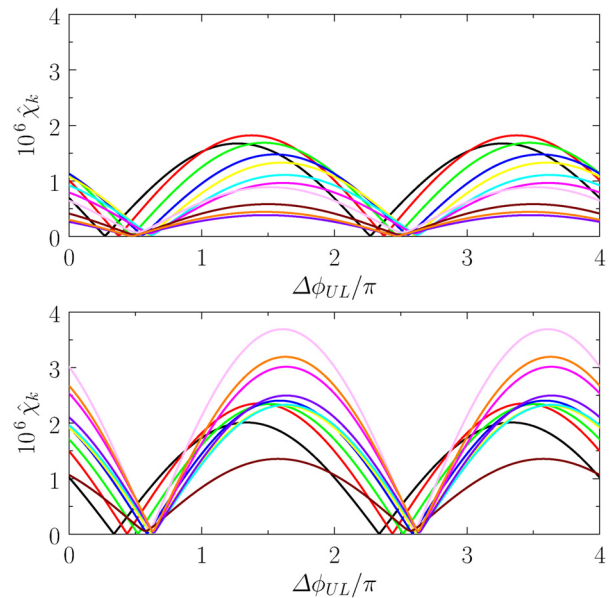


FIG. 5. Normalized resonant components of the RMP at the various resonant surfaces in a model DIII-D plasma equilibrium with $q_{95} = 4.58$ when a 1 kA $n = 2$ current is passed through the upper and lower sections of the I-coil. Here, $\Delta\phi_{UL}$ is the relative phase of the currents passed through the upper and lower sections of the I-coil. The upper and lower panels show cases where $s_{\text{kink}} = \infty$ and $s_{\text{kink}} = 2$, respectively. The black, red, green, blue, yellow, cyan, magenta, pink, brown, purple, and orange curves show the components at the $m = 3, 4, 5, 6, 7, 8, 9, 10, 11, 12$, and 13 resonant surfaces, respectively.

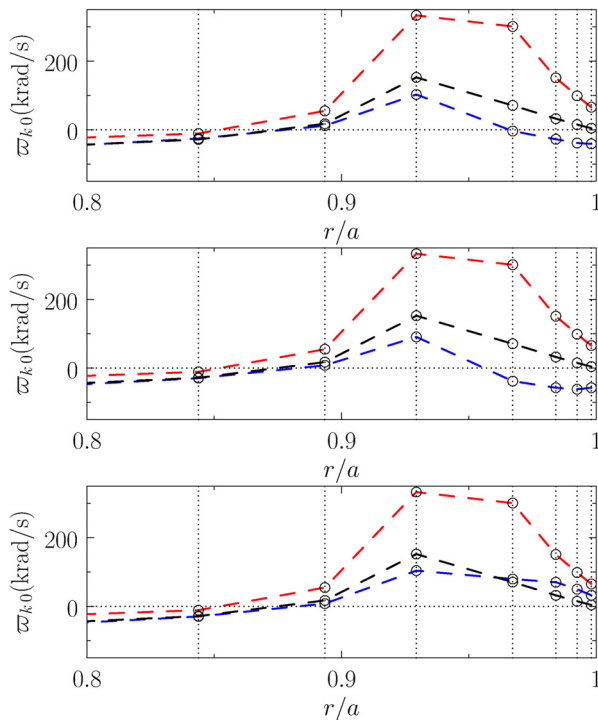


FIG. 6. Natural frequencies at resonant surfaces in the pedestal of a model DIII-D plasma equilibrium with $q_{95} = 4.58$. The points joined by the blue, red, and black dashed lines show the natural frequencies predicted by nonlinear theory, linear theory, and the assumption that a magnetic island chain is convected by the local guiding center fluid, respectively. The top panel shows a calculation in which both plasma impurities and the friction due to charge exchange with neutrals are neglected. The middle panel shows a calculation in which plasma impurities are taken into account, but the friction due to charge exchange with neutrals is neglected. The bottom panel shows a calculation in which both plasma impurities and the friction due to charge exchange with neutrals are taken into account. The vertical lines indicate the positions of the $m=7, 8, 9, 10, 11, 12$, and 13 resonant surfaces, in order from the left to the right.

fluid³⁰) and those calculated on the assumption that magnetic island chains are convected by the local guiding center fluid, are also shown (see Sec. IV). Three cases are considered. In the first case, both plasma impurities and friction due to charge exchange reactions between majority ions and neutrals are neglected in the calculation. In the second case, plasma impurities are taken into account, but charge exchange friction with neutrals is neglected. In the third case, both plasma impurities and charge exchange friction with neutrals are taken into account. It can be seen that, under normal circumstances, the natural frequencies are such that magnetic island chains propagate in the ion diamagnetic direction relative to the local $\mathbf{E} \times \mathbf{B}$ frame (i.e., the points joined by the blue dotted lines lie on the opposite side of the points joined by the black dotted lines to the points joined by the red dotted lines).^{47,48} Plasma impurities cause the natural frequencies to shift slightly in the ion diamagnetic direction relative to the local $\mathbf{E} \times \mathbf{B}$ frame. On the other hand, charge exchange friction with neutrals causes the natural frequencies of resonant surfaces located at the bottom of the pedestal to shift in the electron diamagnetic direction to such an extent that the associated magnetic island chains end up

propagating in the electron diamagnetic direction relative to the local $\mathbf{E} \times \mathbf{B}$ frame (i.e., the points joined by the blue dotted lines lie on the same side of the points joined by the black dotted lines to the points joined by the red dotted lines) (see the discussion in Sec. IV). The incorporation of charge exchange friction with neutrals into the model is clearly important, because, without such friction, the model predicts a spurious zero crossing of the natural frequency at the bottom of the pedestal.

E. Driven island widths

Figure 7 shows the magnetic island widths driven at the resonant surfaces by an $n=2$ I-coil current of 4.2 kA in our model plasma equilibrium (with $s_{\text{kink}} = 2$). The relative phase between the currents flowing in the upper and the lower sections of the I-coil is ramped linearly from $\Delta\phi_{UL} = 0.75\pi$ to $\Delta\phi_{UL} = 2.75\pi$ on a timescale of 1 s. The island widths are averaged over a moving 1 ms time window (otherwise, pulsating island solutions would appear as filled areas—see Ref. 30). The value of the perpendicular momentum diffusivity, $\chi_{\perp} \simeq 1 \text{ m}^2 \text{ s}^{-1}$, is inferred from the TRANSP code⁴⁹ using the measured toroidal rotation of the carbon VI impurities and the known torque input from neutral beams. Neoclassical toroidal viscosity is neglected. The simulation is performed with 200 velocity harmonics [i.e., $P=200$ in Eq. (D2)]. Given that there are 11 resonant surfaces in the plasma, the complete model, (E1)–(E4), consists of 4422 simultaneous first-order ordinary differential equations. Nevertheless, the simulation can be performed in a matter of minutes on a regular laptop or desktop computer.

It is clear from Fig. 7 that driven magnetic reconnection is strongly suppressed by plasma flow at all resonant surfaces apart from the $m=8$, $m=12$, and $m=13$ surfaces. The suppression of driven reconnection fails at the $m=12$ and $m=13$ surfaces, which lie at the bottom of the pedestal, because the plasma there is too cold and resistive for the levels of flow present in this region to give rise to effective suppression of driven reconnection.^{22,30} The suppression of driven

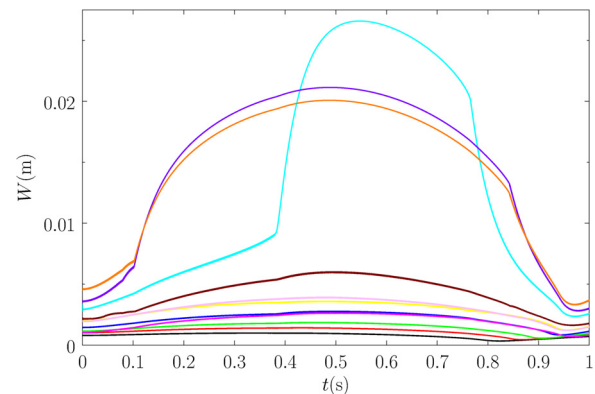


FIG. 7. Magnetic island widths driven by an $n=2$ I-coil current of 4.2 kA at the resonant surfaces in a model DIII-D plasma equilibrium with $q_{95} = 4.58$ and $s_{\text{kink}} = 2$. The relative phase between the currents flowing in the upper and the lower sections of the I-coil is ramped linearly from $\Delta\phi_{UL} = 0.75\pi$ to $\Delta\phi_{UL} = 2.75\pi$ on a timescale of 1 s. The island widths are averaged over a moving 1 ms time window. The black, red, green, blue, yellow, cyan, magenta, pink, brown, purple, and orange curves show the components at the $m=3, 4, 5, 6, 7, 8, 9, 10, 11, 12$, and 13 resonant surfaces, respectively.

reconnection fails at the $m = 8$ surface because the natural frequency at this surface is close to zero—see Fig. 6.^{22,30} It can be seen, by comparison with Fig. 5, that the $m = 12$ and $m = 13$ island widths modulate fairly smoothly with the amplitudes of the resonant components of the RMP. On the other hand, the $m = 8$ island width remains relatively small until the resonant component of the RMP at the $m = 8$ surface exceeds a certain threshold value, at which time the island width suddenly increases. This so-called mode penetration phenomenon is associated with the abrupt generation of a locked magnetic island chain at the $m = 8$ surface.^{22,30} When the resonant component of the RMP falls below a second, somewhat smaller, threshold value, the island chain unlocks, and the $m = 8$ island width suddenly decreases.

F. Temperature and density flattening

As is well known, the plasma temperature and density profiles are flattened across the region that lies inside the separatrix of a magnetic island chain, provided that the full island width exceeds a certain threshold value.⁵⁰ The threshold full magnetic island width at the k th resonant surface above which the electron temperature profile is flattened is⁵⁰

$$W_{T,k} = \left(\frac{\chi_{\perp}}{v_e r_k \epsilon_k s_k n} \right)^{1/3} r_k, \quad (7)$$

where r_k is the r coordinate of the surface, $\epsilon_k = r_k/R_0$, $s_k = (d \ln q / d \ln r)_{r=r_k}$ is the magnetic shear at the surface, $v_e = (T_e/m_e)^{1/2}$ is the local electron thermal speed, and χ_{\perp} is the local particle diffusivity (which is assumed to be the same as the momentum diffusivity). The threshold full magnetic island width at the k th resonant surface above which the electron number density profile (as well as the ion temperature profile) is flattened is⁵⁰

$$W_{n,k} = \left(\frac{\chi_{\perp}}{v_i r_k \epsilon_k s_k n} \right)^{1/3} r_k, \quad (8)$$

where $v_i = (T_i/m_i)^{1/2}$ is the local ion thermal speed and χ_{\perp} is the local energy diffusivity (which is also assumed to be the same as the momentum diffusivity). The previous two expressions take into account the fact that parallel transport in the pedestal of an H-mode tokamak plasma is convective, rather than diffusive, in nature.^{50,51}

If W_k is the full magnetic island width at the k th resonant surface then

$$\bar{W}_k = \frac{2}{\pi} W_k \quad (9)$$

is the mean island width (averaged over the resonant flux surface). Thus, on average, the presence of a magnetic island chain of full width W_k at the k th resonant surface causes the electron temperature to be flattened in an annular region (in r), centered on the resonant surface, of width,

$$\delta_{T,k} = \frac{2}{\pi} W_k \tanh\left(\frac{W_k}{W_{T,k}}\right). \quad (10)$$

Note that the previous equation takes into account the fact that the temperature is only flattened inside the separatrix of the island chain

when W_k exceeds $W_{T,k}$. Similarly, the presence of a magnetic island chain of full width W_k at the k th resonant surface causes the electron number density to be flattened in an annular region (in r), centered on the resonant surface, of width,

$$\delta_{n,k} = \frac{2}{\pi} W_k \tanh\left(\frac{W_k}{W_{n,k}}\right). \quad (11)$$

Following Chang and Callen,⁵² we assume that the temperature flattening at the k th resonant surface causes a shift in the temperature interior to the surface, but does not affect the temperature exterior to the surface, likewise, for the density. Hence, the shift in the electron temperature in the region interior to the k th resonant surface, due to the presence of a magnetic island chain at that surface, is

$$\Delta T_{ek} = \left(\frac{dT_e}{dr} \right)_{r=r_k} \delta_{T,k}. \quad (12)$$

Likewise, the shift in the electron number density in the region interior to the k th resonant surface, due to the presence of a magnetic island chain at that surface, is

$$\Delta n_{ek} = \left(\frac{dn_e}{dr} \right)_{r=r_k} \delta_{n,k}. \quad (13)$$

Figure 8 shows the reductions in the electron number density and the electron temperature in the regions interior to the various resonant surfaces due to the magnetic island chains driven at the surfaces by an $n = 2$ I-coil current of 4.2 kA in our model DIII-D plasma equilibrium (with $s_{\text{sink}} = 2$). The reductions are normalized to the equilibrium electron number density and electron temperature, respectively, at the top of the pedestal (i.e., at the $q = 3$ surface). The relative phase between the currents flowing in the upper and the lower sections of the I-coil is ramped linearly from $\Delta\phi_{UL} = 0.75\pi$ to $\Delta\phi_{UL} = 2.75\pi$ on a timescale of 1 s. The reductions are averaged over a moving 1 ms time window. It can be seen that the density reduction is dominated by the contributions from the $m = 12$ and $m = 13$ resonant surfaces, which are located at the bottom of the pedestal. The next largest contribution comes from the $m = 8$ surface, which is located at the top of the pedestal. On the other hand, many resonant surfaces make significant contributions to the temperature reduction. Note that the cumulative relative reduction in the density is somewhat larger than that in the temperature. Note, further, that about half the density reduction takes place at the bottom of the pedestal (i.e., at the $m = 12$ and $m = 13$ resonant surfaces), whereas the temperature reduction is spread much more evenly across the whole pedestal. The reason for this difference is that the density gradient scale length at the bottom of the pedestal is much less than the temperature gradient scale length. Hence, the flattening of the density and temperature profiles at the $m = 12$ and $m = 13$ surfaces has a disproportionate effect on the density profile immediately interior to these surfaces.^{22,30} We speculate that the temperature gradient scale length at the bottom of the pedestal is increased, relative to the density gradient scale length, by the influx of cold neutrals into the plasma.

Following Refs. 22 and 30, we associate the reduction in the density and temperature profiles due to magnetic island chains driven at the $m = 12$ and $m = 13$ resonant surfaces, which are located at the bottom of the pedestal, with the density pump-out phenomenon. Note that the reduction does indeed vary smoothly with the locally resonant

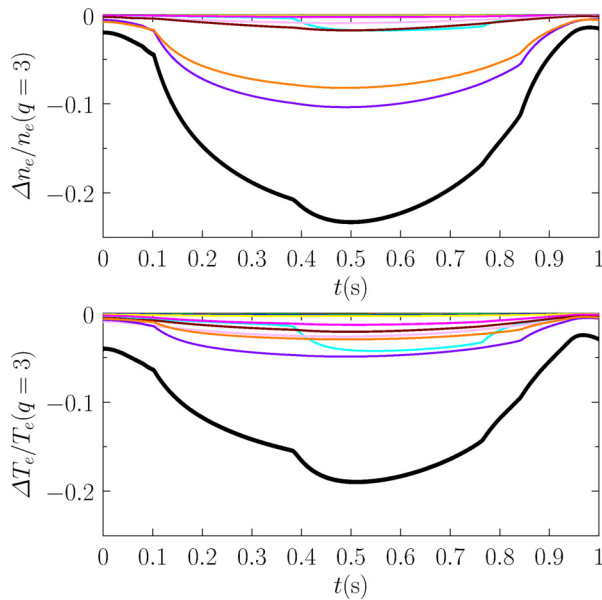


FIG. 8. Relative reduction in the electron number density (top panel) and the electron temperature (bottom panel) in the regions interior to the various resonant surfaces due to the magnetic island chains driven at the surfaces by an $n=2$ I-coil current of 4.2 kA in a model DIII-D plasma equilibrium with $q_{95} = 4.58$ and $s_{\text{kink}} = 2$. The relative phase between the currents flowing in the upper and the lower sections of the I-coil is ramped linearly from $\Delta\phi_{UL} = 0.75\pi$ to $\Delta\phi_{UL} = 2.75\pi$ on a timescale of 1 s. The reductions are averaged over a moving 1 ms time window. The black, red, green, blue, yellow, cyan, magenta, pink, brown, purple, and orange curves show the components at the $m=3, 4, 5, 6, 7, 8, 9, 10, 11, 12$, and 13 resonant surfaces, respectively. The thick black lines show the cumulative relative reductions interior to the innermost resonant surface.

components of the RMP. Moreover, the relative reduction in the density just interior to these surfaces (i.e., in the steep gradient part of the pedestal) is larger than the relative reduction in the temperature.

Again following Refs. 22 and 30, we associate the flattening of the density and temperature profiles at the top of the pedestal, due to mode penetration at the $m=8$ surface, with ELM suppression. Note that the flattening does indeed have a sudden onset when the locally resonant component of the RMP exceeds a certain threshold value. Incidentally, it is not difficult to understand why the flattening of the density and temperature profiles at the top of the pedestal might give rise to ELM suppression. The flattening reduces the pressure gradient at the top of the pedestal, which is likely to move the plasma further from the peeling-ballooning stability threshold.

G. Simulated integrated Mirnov signal

Figure 9 shows the simulated integrated Mirnov signal detected by a toroidal array of pickup coils located on the inboard midplane when an $n=2$ I-coil current of 4.2 kA is applied to our model DIII-D plasma equilibrium (with $s_{\text{kink}} = 2$). The relative phase between the currents flowing in the upper and the lower sections of the I-coil is ramped linearly from $\Delta\phi_{UL} = 0.75\pi$ to $\Delta\phi_{UL} = 2.75\pi$ on a timescale of 1 s. The pickup coil array is located at $R=0.977$ m and $Z=0.00$ m, which is approximately the location of the inboard toroidal array of pickup coils in the DIII-D tokamak. The signal does not

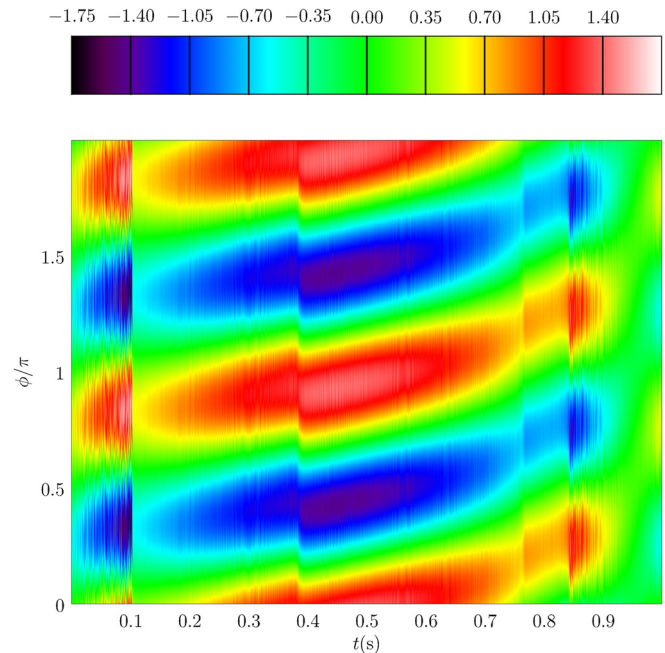


FIG. 9. Simulated integrated Mirnov signal detected by a toroidal array of pickup coils located on the inboard midplane when an $n=2$ I-coil current of 4.2 kA is applied to a model DIII-D plasma equilibrium with $q_{95} = 4.58$ and $s_{\text{kink}} = 2$. The relative phase between the currents flowing in the upper and the lower sections of the I-coil is ramped linearly from $\Delta\phi_{UL} = 0.75\pi$ to $\Delta\phi_{UL} = 2.75\pi$ on a timescale of 1 s. The signal is measured in gauss.

include the vacuum signal generated by the RMP coils. It can be seen (not surprisingly) that the signal has an $n=2$ structure. Prior to mode penetration at the $m=12$ and $m=13$ resonant surfaces, the pickup coils array detects a relatively large amplitude signal generated by the shielding currents at these surfaces. After penetration, the array detects a signal generated by the locked magnetic island chains induced at the $m=12$ and $m=13$ resonant surfaces. The amplitude of this signal increases as the widths of the islands increase. After mode penetration at the $m=8$ surface, the signal is augmented by the signal generated by the locked magnetic island chain generated at that surface.

Figure 10 shows the simulated integrated Mirnov signal detected by a toroidal array of pickup coils located on the outboard midplane for the same case shown in Fig. 9. The pickup coil array is located at $R=2.413$ m, $Z=0.00$ m, which is approximately the location of the outboard toroidal array of pickup coils in the DIII-D tokamak. The signal does not include the vacuum signal generated by the RMP coils. The signal has similar features to that shown in Fig. 9, except that the contribution from the locked island chain generated at the $m=8$ resonant surface, after mode penetration at that surface, is significantly larger in magnitude than the signals generated by shielding currents and locked magnetic island chains at the $m=12$ and $m=13$ resonant surfaces.

The simulated integrated Mirnov data shown in Figs. 9 and 10 are qualitatively similar to those seen on the DIII-D tokamak.¹⁷ In particular, Fig. 10 is similar to Fig. 2(d) in Ref. 17 (provided that we invert the vertical axis to take into account that the toroidal magnetic field in

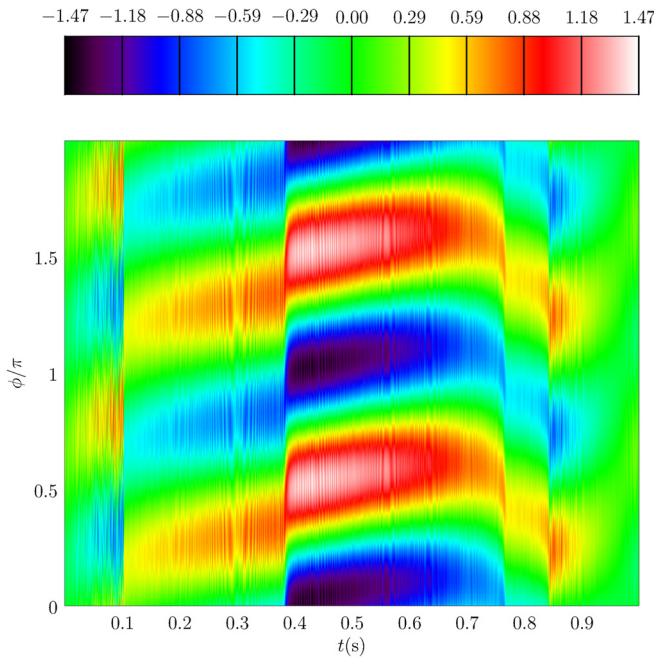


FIG. 10. Simulated integrated Mirnov signal detected by a toroidal array of pickup coils located on the outboard midplane when an $n=2$ I-coil current of 4.2 kA is applied to a model DIII-D plasma equilibrium with $q_{95} = 4.58$ and $s_{\text{kink}} = 2$. The relative phase between the currents flowing in the upper and the lower sections of the I-coil is ramped linearly from $\Delta\phi_{UL} = 0.75\pi$ to $\Delta\phi_{UL} = 2.75\pi$ on a timescale of 1 s. The signal is measured in gauss.

DIII-D is negative). Moreover, the predicted signal levels are similar to those measured on DIII-D.

IV. SAFETY-FACTOR SCAN

In this section, we investigate the dependence of the penetration thresholds at the various resonant surfaces on the locations of these surfaces in a typical DIII-D H-mode plasma subject to an $n=2$ RMP generated by the I-coil. In order to achieve this goal, we make use of the series of self-similar plasma equilibria described in Sec. III A. Figure 11 shows the central safety-factor, q_0 , the 95% normalized magnetic flux safety-factor, q_{95} , and the edge safety-factor, q_a , for these equilibria as functions of q_{95} . It can be seen that q_{95} ranges from about 2.7 to 4.9. Note that q_0 is given a constant value that lies just above unity (because, on average, the central safety-factor is pinned to a value that is close to unity by the sawtooth oscillation). On the other hand, q_a increases with q_{95} . It is obvious that as q_{95} increases more and more $n=2$ resonant surfaces cross the plasma boundary and enter the plasma.

Figure 12 shows the critical $n=2$ I-coil current at which mode penetration occurs at the various resonant surfaces in the series of self-similar tokamak equilibria that feature in Fig. 11 as functions of q_{95} . Here, the I-coil current is ramped linearly from 0 to 5 kA on a timescale of 1 s. Note that 5 kA is the maximum practical current that can be driven through the I-coil. The phase-shift between the currents flowing in the upper and lower sections of the I-coil takes the constant value $\Delta\phi_{UL} = 1.5\pi$ (see Fig. 5). The kink response parameter is given the value $s_{\text{kink}} = 2$. Figure 13 shows the normalized minor radii of the

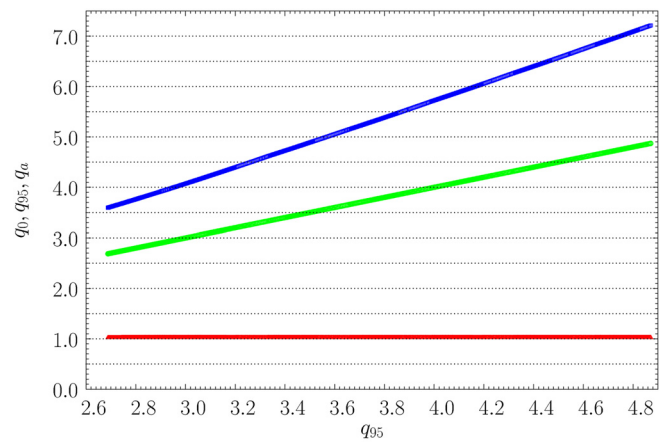


FIG. 11. The central safety-factor, $q_0 \equiv q(\Psi_N = 0)$ (red), the 95% normalized magnetic flux safety-factor, $q_{95} \equiv q(\Psi_N = 0.95)$ (green), and the edge safety-factor $q_a \equiv q(\Psi_N = 1)$ (blue), as functions of q_{95} for a series of self-similar tokamak equilibria with the same shape and pressure profile as DIII-D discharge #158115 at time $t = 3250$ ms.

various resonant surfaces at which mode penetration occurs for the cases shown in Fig. 12. It can be seen that mode penetration only occurs for resonant surfaces that lie at the bottom of the pedestal (i.e., $0.98 \leq r/a \leq 1$) or at the top of the pedestal (i.e., $0.88 \leq r/a \leq 0.92$). Mode penetration takes place at the bottom of the pedestal because the plasma there is too cold and resistive for the levels of plasma flow present in this region to give rise to effective shielding of driven magnetic reconnection.^{22,30} Mode penetration takes place at the top of the pedestal because the natural frequency of the relevant resonant surface is close to zero (see Fig. 13).^{22,30} For example, mode penetration at the $q=4$ surface (cyan points) takes place for $3.0 < q_{95} < 3.6$ because the surface is located in the relatively cold plasma at the bottom of the pedestal. On the other hand, mode penetration at the $q=4$ surface takes place for $4.55 < q_{95} < 4.81$ because the surface is located close to the top of the pedestal where the natural frequency passes through zero.

Assuming that mode penetration at the top of the pedestal is a necessary condition for ELM suppression,^{22,30} it is clear from Figs. 12 and 13 that there are four q_{95} windows for $2.6 < q_{95} < 4.9$ in which $n=2$ RMP-induced ELM suppression could occur in DIII-D H-mode discharges. The first window corresponds to $2.75 < q_{95} < 2.98$ and is associated with mode penetration at the $m=5$ resonant surface. The second window corresponds to $3.30 < q_{95} < 3.59$ and is associated with mode penetration at the $m=6$ resonant surface. The third window corresponds to $3.91 < q_{95} < 4.20$ and is associated with mode penetration at the $m=7$ resonant surface. The fourth window corresponds to $4.55 < q_{95} < 4.81$ and is associated with mode penetration at the $m=8$ resonant surface.

It can be seen from Fig. 12 that the critical I-coil current required to produce mode penetration at the top of the pedestal falls to zero in the middle of each of the aforementioned four q_{95} windows. At first sight, this might seem to imply that the critical I-coil current required for RMP-induced ELM suppression also falls to zero. However, this is not correct. According to our model, in addition to generating a locked magnetic island chain at the top of the pedestal, in order to suppress ELMs,

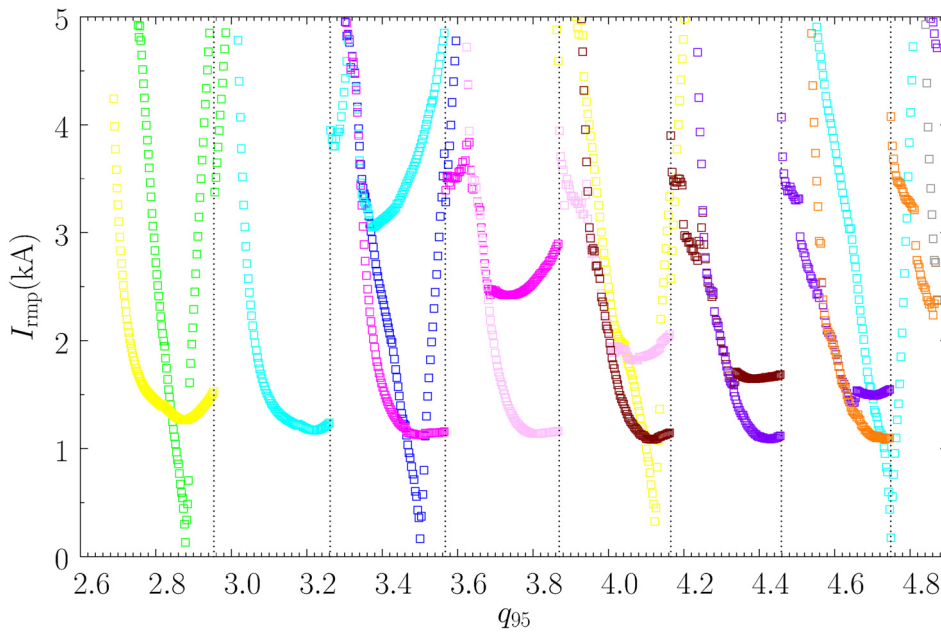


FIG. 12. The critical $n=2$ I-coil currents at which mode penetration occurs at the various resonant surfaces in the series of self-similar tokamak equilibria that feature in Fig. 11 as functions of q_{95} . The I-coil current is ramped linearly from 0 to 5 kA on a timescale of 1 s. The phase-shift between the currents flowing in the upper and lower sections of the I-coil takes the constant value $\Delta\phi_{UL} = 1.5\pi$. The kink response parameter is given the value $S_{\text{kink}} = 2$. The black, red, green, blue, yellow, cyan, magenta, pink, brown, purple, orange, and gray curves show the components at the $m=3, 4, 5, 6, 7, 8, 9, 10, 11, 12, 13$, and 14 resonant surfaces, respectively. The vertical dotted lines show the q_{95} values at which the $m=8, 9, 10, 11, 12, 13$, and 14 resonant surfaces cross the plasma boundary, in order from the left to the right.

the RMP must also generate an island chain that is sufficiently wide to flatten the local temperature and density profiles (see Sec. III F).^{22,30} Hence, even in the middles of the q_{95} windows, the critical I-coil current for RMP-induced ELM suppression remains (small but) finite.

Note, from Fig. 12, that the various critical I-coil currents at which mode penetration occurs change discontinuously each time a new resonant surface enters the plasma. The reason for this is that there are no shielding currents at the resonant surface in question when it lies just outside the plasma. On the other hand, strong

shielding currents can be induced on the surface as soon as it enters the plasma. Given that all of the different poloidal harmonics in the problem are coupled together electromagnetically, these shielding currents are able to modify the mode penetration thresholds at interior resonant surfaces.

The nonlinear magnetic island theory employed in this paper, according to which magnetic island chains are effectively entrained by the ion fluid, yields the following expression for the natural frequency at the k th resonant surface:

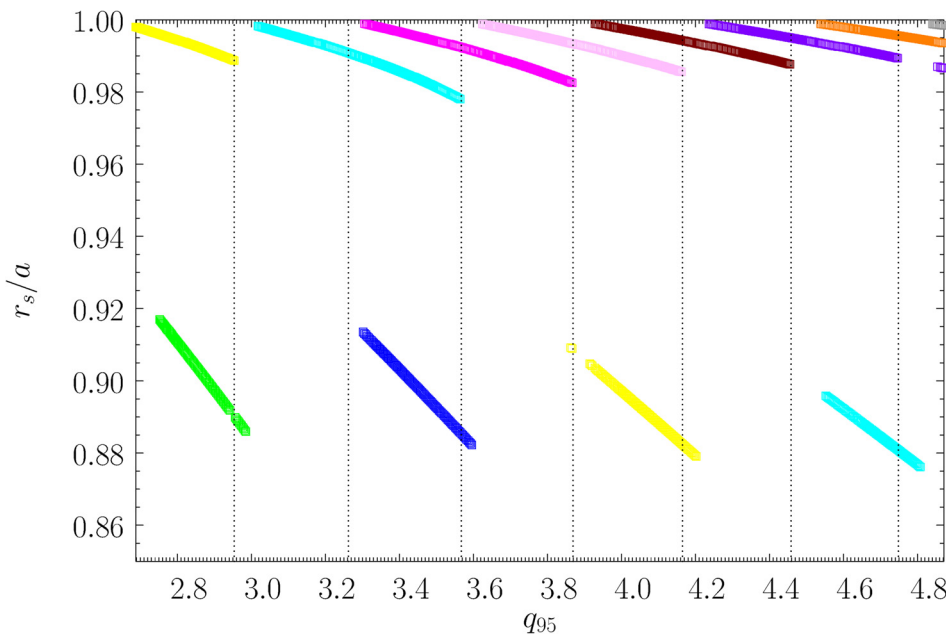


FIG. 13. The normalized radii of the various resonant surfaces at which mode penetration occurs for the calculations shown in Fig. 12. The green, blue, yellow, cyan, magenta, pink, brown, purple, orange, and gray curves show the components at the $m=5, 6, 7, 8, 9, 10, 11, 12, 13$, and 14 resonant surfaces, respectively.

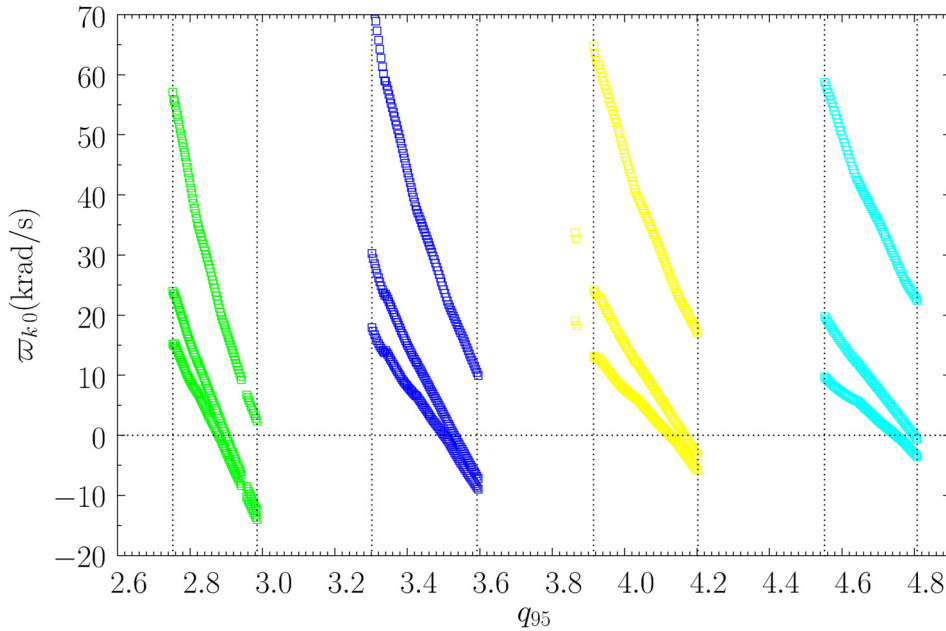


FIG. 14. The natural frequencies of the various resonant surfaces at the top of the pedestal at which mode penetration occurs for the calculations shown in Fig. 12. The green, blue, yellow, and cyan curves show the natural frequencies at the $m=5, 6, 7$, and 8 resonant surfaces, respectively. The vertical dotted lines indicate the boundaries of the q_{95} windows. The upper, middle, and lower curves correspond to $\varpi_{k0} = \varpi_{k0\text{linear}}$, $\varpi_{k0} = \varpi_{k0E}$, and $\varpi_{k0} = \varpi_{k0\text{nonlinear}}$, respectively.

$$\varpi_{k0\text{nonlinear}} = -n \left(\omega_E + \left[1 - L_{00}^{ii} + L_{01}^{ii} \left(\frac{\eta_i}{1 + \eta_i} \right) \right] \omega_{*i} - \left[L_{00}^{il} - L_{01}^{il} \left(\frac{\eta_I}{1 + \eta_I} \right) \right] \omega_{*I} \right)_{r_k}, \quad (14)$$

where

$$\omega_E(r) = -\frac{1}{B_0} \frac{q}{g} \frac{1}{r} \frac{d\Phi}{dr}, \quad (15)$$

$$\omega_{*a}(r) = -\frac{T_a}{e_a B_0} \frac{q}{g} \frac{1}{r} \frac{d \ln p_a}{dr}, \quad (16)$$

$$\eta_a(r) = \frac{d \ln T_a}{d \ln n_a}. \quad (17)$$

Here, $\Phi(r)$ is the electric scalar potential, $g(r)$ is defined in Appendix A 2, and e_a , $n_a(r)$, $T_a(r)$, and $p_a(r)$ are the electrical charge, number density, temperature, and pressure of the plasma species a , respectively. [The three species are electrons (e), majority ions (i), and

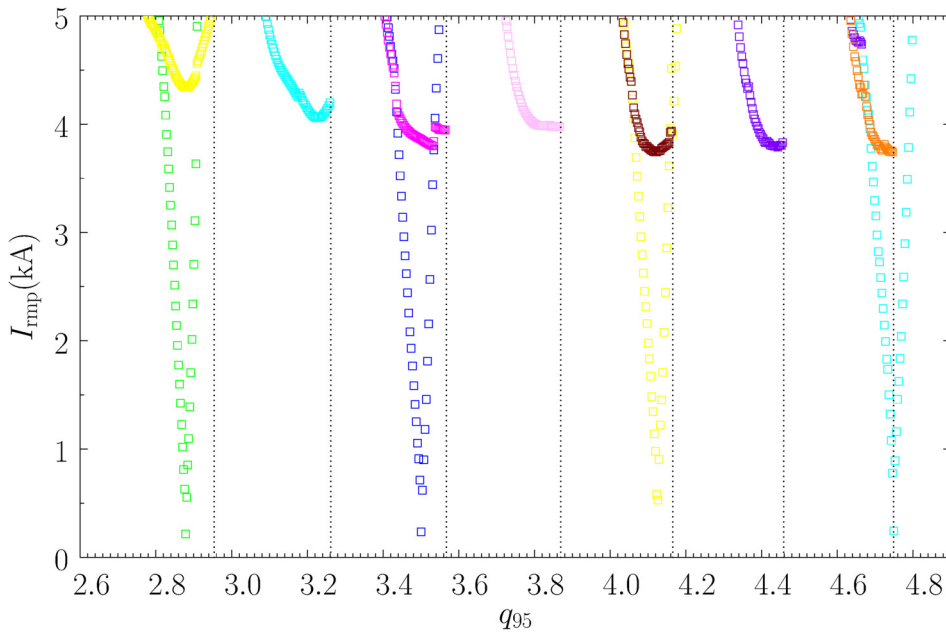


FIG. 15. The critical $n=2$ I-coil currents at which mode penetration occurs at the various resonant surfaces in the series of self-similar tokamak equilibria that feature in Fig. 11 as functions of q_{95} . The I-coil current is ramped linearly from 0 to 5 kA on a timescale of 1 s. The phase-shift between the currents flowing in the upper and lower sections of the I-coil takes the constant value $\Delta\phi_{UL} = 1.5\pi$. The kink response parameter is given the value $S_{\text{kink}} = 8$. The green, blue, yellow, cyan, magenta, pink, brown, purple, and orange curves show the components at the $m=5, 6, 7, 8, 9, 10, 11, 12$, and 13 resonant surfaces, respectively.

impurity ions (I .) On the other hand, if the plasma response at the k th resonant surface were governed by linear layer physics, according to which magnetic island chains are effectively entrained by the electron fluid, then the expression for the natural frequency would be

$$\varpi_{k0\text{linear}} = -n(\omega_E + \omega_{*e})_{r_k}. \quad (18)$$

Finally, if magnetic island chains were entrained by the guiding center fluid then the expression for the natural frequency at the k th resonant surface would be

$$\varpi_{k0E} = -n(\omega_E)_{r_k}. \quad (19)$$

Note, incidentally, that, in the limit in which charge exchange friction with neutrals is dominant, expression (14) reduces to

$$\varpi_{k0\text{nonlinear}} = -n[\omega_E + (1 - y_n)\omega_{*i}]_{r_k}. \quad (20)$$

Thus, charge exchange causes the natural frequency to shift in the electron diamagnetic direction relative to the $\mathbf{E} \times \mathbf{B}$ frequency provided $y_n > 1$ (i.e., provided the neutral density peaks poloidally in the vicinity of the X-point) [see Eq. (5)]. On the other hand, if the neutral density were to be lower than average in the vicinity of the X-point then charge exchange friction would cause the natural frequency to shift in the ion diamagnetic direction.

Figure 14 shows the $\varpi_{k0\text{nonlinear}}$, $\varpi_{k0\text{linear}}$, and ϖ_{k0E} values associated with mode penetration at the top of the pedestal in the four q_{95} windows that are apparent in Figs. 12 and 13. It can be seen that $\varpi_{k0\text{nonlinear}}$ crosses zero in the middle of each window, which is consistent with the idea that mode penetration at the top of the pedestal in DIII-D H-mode discharges is triggered when the (nonlinear) natural frequency at a resonant surface in that region becomes small. Note that $\varpi_{k0\text{linear}}$ does not pass through zero in any of the q_{95} windows. On the other hand, ϖ_{k0E} (which is not too dissimilar to $\varpi_{k0\text{nonlinear}}$) passes through zero in each window. In fact, in a recent experimental study,

it was concluded that RMP-induced ELM suppression in DIII-D H-mode discharges is not correlated with $\varpi_{k0\text{linear}}$ passing through zero at the top of the pedestal, but is correlated with ϖ_{k0E} passing through zero in the same region.¹⁶

Figures 15 and 16 show analogous data to Figs. 12 and 13, except that the kink parameter has been given the value $s_{\text{kink}} = 8$. Similarly, Figs. 17 and 18 show analogous data to Figs. 12 and 13, except that the kink parameter has been given the value $s_{\text{kink}} = \infty$. It can be seen that as the kink response of the plasma becomes weaker (i.e., as $1/s_{\text{kink}} \rightarrow 0$) the critical I-coil current needed to induce locked magnetic island chains becomes larger, and the widths of the q_{95} windows within which mode penetration at the top of the pedestal is possible shrink. In the complete absence of plasma amplification of the RMP, due to the kink response, (i.e., $s_{\text{kink}} = \infty$) the maximum practical I-coil current (i.e., 5 kA) is insufficient to induce locked magnetic island chains at the bottom of the pedestal. Moreover, the widths of the q_{95} windows within which mode penetration at the top of the pedestal is possible are miniscule. We deduce that, were it not for the amplification of the RMP by the plasma that is associated with the kink response, the I-coil system would not be powerful enough to induce either a density pump-out or ELM suppression in DIII-D H-mode plasmas. Clearly, in order to be successful, an RMP-induced ELM suppression coil system must generate a magnetic field that is simultaneously strongly amplified by the plasma and has a large resonant component at a rational surface that lies close to the top of the pedestal.

V. CONCLUSIONS

The theoretical results presented in Refs. 22 and 30, and in this paper, provide a framework within which most of the salient features of RMP-induced ELM suppression in tokamak H-mode discharges can be understood. In particular, the following conclusions can be drawn from Refs. 22 and 30 and the present paper.

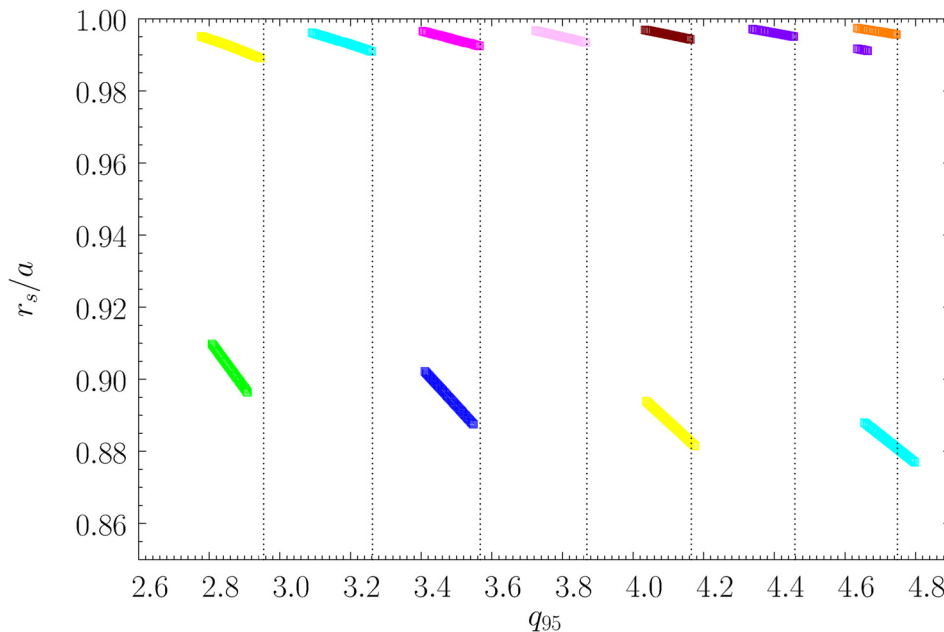


FIG. 16. The normalized radii of the various resonant surfaces at which mode penetration occurs for the calculations shown in Fig. 15. The green, blue, yellow, cyan, magenta, pink, brown, purple, and orange curves show the components at the $m = 5, 6, 7, 8, 9, 10, 11, 12$, and 13 resonant surfaces, respectively.

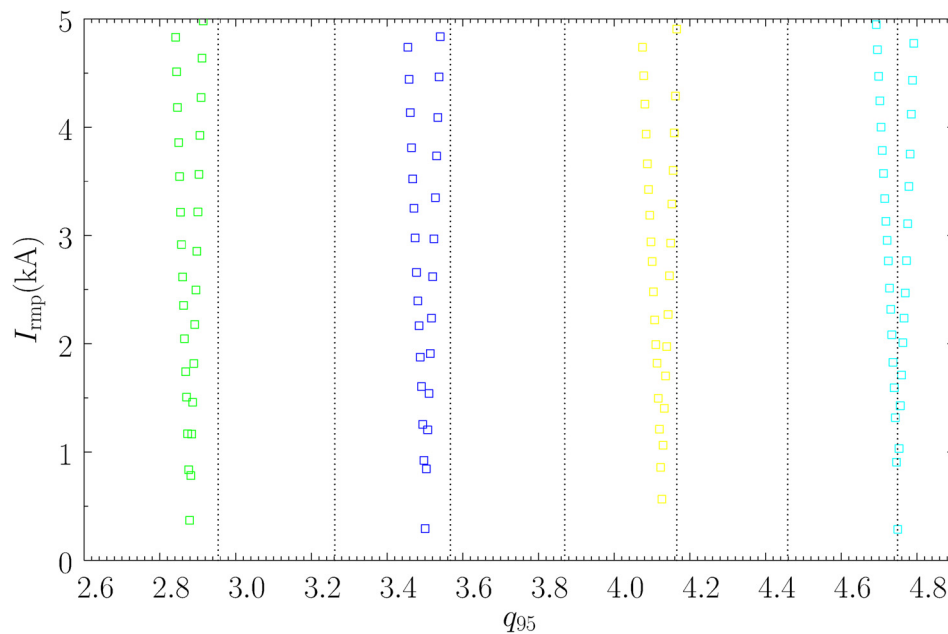


FIG. 17. The critical $n=2$ I-coil currents at which mode penetration occurs at the various resonant surfaces in the series of self-similar tokamak equilibria that feature in Fig. 11 as functions of q_{95} . The I-coil current is ramped linearly from 0 to 5 kA on a timescale of 1 s. The phase-shift between the currents flowing in the upper and lower sections of the I-coil takes the constant value $\Delta\phi_{UL} = 1.5\pi$. The kink response parameter is given the value $S_{\text{kink}} = \infty$. The green, blue, yellow, and cyan curves show the components at the $m=5, 6, 7$, and 8 resonant surfaces, respectively.

1. (As a reminder, a toroidal tokamak equilibrium exhibits two distinct types of response to an applied RMP, namely, the tearing response and the kink response. The tearing response is a non-ideal-MHD response that is associated with the formation of current sheets and magnetic island chains at various resonant surfaces within the plasma. The kink response is an edge-localized ideal-MHD response that is associated with coupling to a stable non-resonant kink mode. The kink response is also associated with the amplification of the applied RMP by the plasma.)

The tearing response at the various magnetic flux-surfaces within the plasma that resonate with the helical harmonics of the RMP is governed by “nonlinear magnetic island physics,” rather than by “linear layer physics.” The reason for this is that the shielding of driven magnetic reconnection by plasma flow in a typical H-mode tokamak discharge is not sufficiently strong to reduce the RMP-induced magnetic island widths below the very narrow associated linear layer widths, which is a necessary condition for the validity of linear theory.³⁰

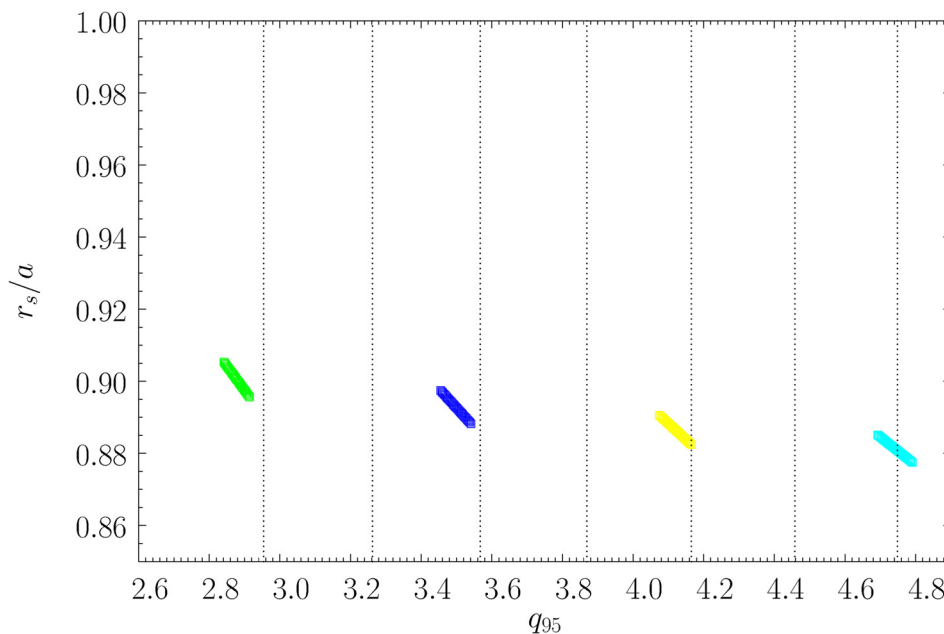


FIG. 18. The normalized radii of the various resonant surfaces at which mode penetration occurs for the calculations shown in Fig. 17. The green, blue, yellow, and cyan curves show the components at the $m=5, 6, 7$, and 8 resonant surfaces, respectively.

2. The shielding of driven magnetic reconnection by plasma flow in a typical H-mode tokamak discharge is sufficiently strong to prevent the formation of RMP-driven locked magnetic island chains at all resonant surfaces in the plasma except for those that lie at the bottom and at the top of the pedestal (see Fig. 7). (Note that, except possibly at the bottom of the pedestal, a magnetic island chain can only overcome the shielding effect of plasma flow by locking to the RMP.) The shielding fails at the bottom of the pedestal because the plasma is too cold and resistive for the levels of flow present in this region to give rise to effective suppression of driven reconnection. The shielding fails at the top of the pedestal because the natural frequency (i.e., the helical phase velocity of a naturally unstable magnetic island chain) passes through zero close to the top of the pedestal (see Fig. 5). Note that the degree of shielding of driven magnetic reconnection by plasma flow is proportional to the local natural frequency. Incidentally, the reason that the natural frequency inevitably passes through zero close to the top of the pedestal of a conventional H-mode tokamak plasma is that the radial electric field in the pedestal is large [compared to $T_e/(ea)$] and “negative” due to ion orbit losses, whereas that in the plasma core is large and “positive” due to the fact that toroidal momentum is usually injected into the core (via neutral beam heating) in the same direction as the toroidal plasma current (see Figs. 2 and 3).
 3. The natural frequency is largely determined by neoclassical physics (through the neoclassical stress tensor).⁴⁵ The levels of plasma impurities present in a typical tokamak H-mode plasma are sufficiently high to have a slight effect on the natural frequency (see Fig. 6). Furthermore, the levels of neutrals present at the edge of a typical tokamak H-mode discharge are sufficiently high that friction due to charge exchange reactions between majority ions and these neutrals has a very significant effect on the natural frequency at the bottom of the pedestal (see Fig. 6).
 4. The density pump-out phenomenon is hypothesized to be associated with the flattening of the plasma density and temperature at the bottom of the pedestal due to the formation of RMP-induced locked magnetic island chains in this region. The degree of flow shielding at the bottom of the pedestal is relatively weak, because the plasma there is comparatively cold and resistive. Consequently, the widths of the driven island chains are roughly proportional to the square-roots of the amplitudes of the locally resonant components of the RMP (which is the scaling that would be expected in the absence of shielding) (see Figs. 5 and 7). Because the electron number density gradient scale length is significantly less than the electron temperature gradient scale length at the bottom of the pedestals of typical present-day H-mode tokamak plasmas (see Fig. 3), the flattening of the density and the temperature across the aforementioned RMP-induced magnetic island chains causes a much larger relative decrease in the pedestal density in the region immediately interior to these surfaces than it does in the pedestal temperature (see Fig. 8). We speculate that the electron temperature gradient scale length at the bottom of a typical H-mode tokamak plasma pedestal is larger than the electron number density gradient scale length because of the influx of cold neutrals. Note that not all experiments show a clear decrease in the pedestal temperature during the density pump-out. Such observations are difficult for the model presented in this paper to explain. An alternative explanation for the density pump-out is that it is due to RMP-modified turbulent transport. However, it is not clear why such transport should affect particles much more strongly than energy.
 5. The ELM suppression phenomenon is hypothesized to be associated with locked magnetic island formation at the top of the pedestal. The degree of flow shielding at the top of the pedestal is such that locked island formation is only possible if the magnitude of the natural frequency at the relevant resonant surface takes a comparatively small value (i.e., less than 10 krad/s in typical DIII-D H-mode tokamak discharges) (see Fig. 14). This, in turn, is only possible if q_{95} lies in certain narrow windows, which ensures that the resonant surface lies close to the zero crossing of the natural frequency (see Fig. 13). This offers an explanation for why ELM suppression only takes place when q_{95} lies in certain narrow windows. A critical RMP coil current, that is roughly proportional to the natural frequency, must be exceeded before a locked island chain can be induced at the resonant surface. The critical RMP coil current needed to induce ELM suppression remains finite, even in the middle of the q_{95} window where the natural frequency is exactly zero, because, according to our model, in order to suppress ELMs, the locked magnetic island chain induced at the top of the pedestal must be sufficiently wide to flatten the local density and temperature profiles (see Sec. III F). We speculate that ELM mitigation (as opposed to complete ELM suppression) corresponds to a situation in which a locked island chain is induced at the top of the pedestal, but is not wide enough to completely flatten the density and temperature profiles. The $\mathbf{E} \times \mathbf{B}$ frequency, ω_E , passes through zero in the q_{95} windows, but the perpendicular electron frequency, $\omega_{\perp e} \equiv \omega_E + \omega_{*e}$, does not.¹⁶ (See Fig. 14.)
 6. In order to successfully induce a locked magnetic island chain at the top of the pedestal, an RMP-induced ELM suppression coil system must generate a magnetic field that is simultaneously strongly amplified by the plasma (via the kink response) and has a large resonant component at a rational surface that lies close to the top of the pedestal.
- In the ITER tokamak, we expect the temperature at the bottom of the pedestal to be significantly larger than in present-day tokamaks. We also expect the relative distance that the neutrals penetrate inside the LCFS, and the degree of poloidal asymmetry of the neutral distribution, to be significantly smaller than in present-day tokamaks. All of these facts point to the possibility that the response of the plasma at the bottom of the pedestal to RMPs in ITER may be quite different to that seen in present-day tokamaks. If the hypothesis of this paper is correct, then this also implies that the density pump-out could be quite different.

ACKNOWLEDGMENTS

This research was funded by the U.S. Department of Energy under Contract Nos. DE-FG02-04ER-54742 and DE-AC02-09CH11466. One of the authors (R.F.) would like to acknowledge helpful discussions with Q. M. Hu, R. Nazikian, S. Mordijck, N. C. Logan, J.-K. Park, and C. Paz-Soldan.

APPENDIX A: ELECTROMAGNETIC PLASMA RESPONSE IN THE OUTER REGION

1. Coordinates

Let R , ϕ , and Z be right-handed cylindrical coordinates whose symmetry axis corresponds to the toroidal symmetry axis of the plasma. Let r , θ , and ϕ be right-handed flux coordinates whose Jacobian is

$$\mathcal{J} \equiv (\nabla r \times \nabla \theta \cdot \nabla \phi)^{-1} = \frac{r R^2}{R_0}. \quad (\text{A1})$$

Here, R_0 is a convenient scale major radius, r is a magnetic flux-surface label with dimensions of length, and θ is an angular coordinate that increases by 2π radians for every poloidal circuit of the magnetic axis. (Both r and θ are independent of ϕ .) Let $r=0$ correspond to the magnetic axis, and let $r=a$ correspond to the last closed magnetic flux-surface. Let $\theta=0$ correspond to the inboard midplane, and let $0 < \theta < \pi$ correspond to the region above the midplane.

2. Equilibrium magnetic field

The equilibrium magnetic field is written as

$$\mathbf{B} = B_0 R_0 [f(r) \nabla \phi \times \nabla r + g(r) \nabla \phi], \quad (\text{A2})$$

where B_0 is a convenient scale toroidal magnetic field-strength, and

$$q(r) = \frac{r g}{R_0 f} \quad (\text{A3})$$

is the safety-factor profile. The equilibrium poloidal magnetic flux, $\Psi_p(r)$, satisfies

$$\frac{d\Psi_p}{dr} = 2\pi B_0 R_0 f(r), \quad (\text{A4})$$

where, by convention, $\Psi_p(a) = 0$. The normalized poloidal magnetic flux, $\Psi_N(r)$, is defined such that $\Psi_N(r) = 1 - \Psi_p(r)/\Psi_p(0)$. Hence, $\Psi_N(0) = 0$ and $\Psi_N(a) = 1$.

3. Perturbed magnetic field

The perturbed magnetic field satisfies $\nabla \cdot \delta \mathbf{B} = 0$, which can be written as

$$\frac{\partial(\mathcal{J} \delta B^r)}{\partial r} + \frac{\partial(\mathcal{J} \delta B^\theta)}{\partial \theta} + \frac{\partial(\mathcal{J} \delta B^\phi)}{\partial \phi} = 0. \quad (\text{A5})$$

Note that, in this section, unless explicitly stated otherwise, subscript/superscript r , θ , and ϕ refer to covariant/contravariant components of a vector in the r , θ , and ϕ coordinate system.

It is easily demonstrated that

$$\delta B_r = \left(\frac{1}{|\nabla r|^2} \right) \delta B^r - \left(\frac{\nabla r \cdot \nabla \theta}{|\nabla r|^2} \right) \delta B_\theta, \quad (\text{A6})$$

$$\delta B^\theta = \left(\frac{\nabla r \cdot \nabla \theta}{|\nabla r|^2} \right) \delta B^r + \left(\frac{R_0^2}{r^2 R^2 |\nabla r|^2} \right) \delta B_\theta. \quad (\text{A7})$$

Consider the response of the plasma to an RMP harmonic with m periods in the poloidal direction and $n > 0$ periods in the

toroidal direction. If the RMP is resonant in the pedestal of an H-mode tokamak discharge, then it is inevitably the case that $m \gg n$ (because $q \gg 1$ in such a pedestal). (Note that, in this paper, for the sake of simplicity, we are assuming that the helicity of the equilibrium magnetic field is such that $g, f, q > 0$, which implies that all resonant poloidal mode numbers are positive.) It is a fundamental premise of this paper that, in the high- q limit, the curl of the perturbed magnetic field is negligible between resonant surfaces. In other words,

$$\frac{\partial \delta B_\phi}{\partial \theta} \simeq \frac{\partial \delta B_\theta}{\partial \phi}, \quad (\text{A8})$$

$$\frac{\partial \delta B_\theta}{\partial r} \simeq \frac{\partial \delta B_r}{\partial \theta}. \quad (\text{A9})$$

Equations (A8) and (A9) imply that

$$\delta B_\phi \sim \frac{n}{m} \delta B_\theta, \frac{n}{m} r \delta B_r \quad (\text{A10})$$

and, hence, that

$$\delta B^\phi \sim \left(\frac{r}{R} \right)^2 \frac{n}{m} \delta B^\theta, \left(\frac{r}{R} \right)^2 \frac{n}{m} \frac{\delta B^r}{r}. \quad (\text{A11})$$

Consequently, if $q \gg 1$ then the final term on left-hand side of Eq. (A5) is of order $(n/m)^2 (r/R)^2$ smaller than the other two terms, and is, therefore, negligible. Thus, we obtain

$$r \frac{\partial}{\partial r} \left(\frac{r R^2 \delta B^r}{R_0^2} \right) \simeq - \frac{\partial}{\partial \theta} \left[\left(\frac{r \nabla r \cdot \nabla \theta}{|\nabla r|^2} \right) \left(\frac{r R^2 \delta B^r}{R_0^2} \right) + \left(\frac{1}{|\nabla r|^2} \right) \delta B_\theta \right], \quad (\text{A12})$$

where use has been made of Eqs. (A1), (A6), and (A7). Furthermore, Eq. (A9) yields

$$r \frac{\partial \delta B_\theta}{\partial r} \simeq \frac{\partial}{\partial \theta} \left[\left(\frac{R_0^2}{R^2 |\nabla r|^2} \right) \left(\frac{r R^2 \delta B^r}{R_0^2} \right) - \left(\frac{r \nabla r \cdot \nabla \theta}{|\nabla r|^2} \right) \delta B_\theta \right]. \quad (\text{A13})$$

Let

$$\frac{r R^2 \delta B^r(r, \theta, \phi)}{R_0^2} = i \sum_j \psi_j(r) e^{i(m_j \theta - n \phi)}, \quad (\text{A14})$$

$$\delta B_\theta(r, \theta, \phi) = - \sum_j \chi_j(r) e^{i(m_j \theta - n \phi)}, \quad (\text{A15})$$

where the sum is over all relevant poloidal harmonics of the perturbed magnetic field. Incidentally, all harmonics are assumed to possess a common toroidal mode number, $n > 0$. Operating on Eqs. (A12) and (A13) with $\oint (\dots) d\theta/2\pi$, we obtain

$$r \frac{d\psi_j}{dr} \simeq m_j \sum_{j'} (-c_{jj'} \psi_{j'} + a_{jj'} \chi_{j'}), \quad (\text{A16})$$

$$r \frac{d\chi_j}{dr} \simeq m_j \sum_{j'} (-c_{jj'} \chi_{j'} + b_{jj'} \psi_{j'}), \quad (\text{A17})$$

where

$$a_{jj'}(r) = \oint \frac{1}{|\nabla r|^2} e^{-i(m_j - m_{j'})\theta} \frac{d\theta}{2\pi}, \quad (\text{A18})$$

$$b_{jj'}(r) = \oint \frac{R_0^2}{R^2 |\nabla r|^2} e^{-i(m_j - m_{j'})\theta} \frac{d\theta}{2\pi}, \quad (\text{A19})$$

$$c_{jj'}(r) = \oint \frac{i r \nabla r \cdot \nabla \theta}{|\nabla r|^2} e^{-i(m_j - m_{j'})\theta} \frac{d\theta}{2\pi}. \quad (\text{A20})$$

However, we can also obtain Eqs. (A16) and (A17) by taking the limit $m \gg n$ and $|m - nq| \gg 1$ in the completely general analysis presented in Appendix A of Ref. 29. This observation offers some justification for the aforementioned fundamental premise.

Finally, it is readily demonstrated that

$$\frac{r R^2 \delta B^\theta(r, \theta, \phi)}{R_0^2} = - \sum_j \frac{1}{m_j} \frac{d\psi_j}{dr} e^{i(m_j \theta - n\phi)}, \quad (\text{A21})$$

$$R^2 \delta B^\phi(r, \theta, \phi) = n \sum_j \frac{\chi_j(r)}{m_j} e^{i(m_j \theta - n\phi)}, \quad (\text{A22})$$

$$\delta B_r(r, \theta, \phi) = i \sum_j \frac{1}{m_j} \frac{d\chi_j}{dr} e^{i(m_j \theta - n\phi)}, \quad (\text{A23})$$

$$\delta B_\phi(r, \theta, \phi) = n \sum_j \frac{\chi_j(r)}{m_j} e^{i(m_j \theta - n\phi)}. \quad (\text{A24})$$

4. Perturbed current density

Let $\delta \mathbf{J}$ be the perturbed current density. We can write

$$\mathcal{J} \mu_0 \delta J^r = \frac{\partial \delta B_\phi}{\partial \theta} - \frac{\partial \delta B_\theta}{\partial \phi}, \quad (\text{A25})$$

$$\mathcal{J} \mu_0 \delta J^\theta = \frac{\partial \delta B_r}{\partial \phi} - \frac{\partial \delta B_\phi}{\partial r}, \quad (\text{A26})$$

$$\mathcal{J} \mu_0 \delta J^\phi = \frac{\partial \delta B_\theta}{\partial r} - \frac{\partial \delta B_r}{\partial \theta}. \quad (\text{A27})$$

Normally, all three contravariant components of $\delta \mathbf{J}$ are zero. Consider, however, the behavior in the vicinity of the k th resonant surface, $r = r_k$, at which $nq(r_k) = m_k$. In general, ψ_k , $\psi_{j \neq k}$, and $\chi_{j \neq k}$ are continuous across the surface, whereas χ_k is discontinuous.^{25,29} Hence, we deduce that

$$\mathcal{J} \mu_0 \delta J^r(r, \theta, \phi) = 0, \quad (\text{A28})$$

$$\mathcal{J} \mu_0 \delta J^\theta(r, \theta, \phi) = - \sum_{k=1, K} \frac{n}{m_k} [\chi_k]_{r_{k-}}^{r_{k+}} \delta(r - r_k) e^{i(m_k \theta - n\phi)}, \quad (\text{A29})$$

$$\mathcal{J} \mu_0 \delta J^\phi(r, \theta, \phi) = - \sum_{k=1, K} [\chi_k]_{r_{k-}}^{r_{k+}} \delta(r - r_k) e^{i(m_k \theta - n\phi)}, \quad (\text{A30})$$

where use has been made of Eqs. (A15) and (A24). Here, it is assumed that there are K resonant surfaces in the plasma, numbered sequentially from one to K , on the order of the innermost to the outermost. It is easily demonstrated from Eqs. (A2) and (A28)–(A30) that $\delta \mathbf{J} \times \mathbf{B} = \mathbf{0}$ at a given resonant surface [see Eq. (A73)]. Thus, we conclude that a current sheet forms at each resonant surface in the plasma. Moreover, these sheets are made up of current filaments that run parallel to the local equilibrium magnetic field.

5. Electromagnetic torques

We can write

$$(\mu_0 \delta \mathbf{J} \times \delta \mathbf{B})_\theta = \frac{1}{4} (\mathcal{J} \mu_0 \delta J^\phi \delta B^{r*} + \text{c.c.}), \quad (\text{A31})$$

$$(\mu_0 \delta \mathbf{J} \times \delta \mathbf{B})_\phi = \frac{1}{4} (-\mathcal{J} \mu_0 \delta J^\theta \delta B^{r*} + \text{c.c.}) \quad (\text{A32})$$

which implies that

$$\mathcal{J} (\mu_0 \delta \mathbf{J} \times \delta \mathbf{B})_\theta = \frac{R_0}{2} \sum_{k,j} \text{Re} \left\{ i [\chi_k]_{r_{k-}}^{r_{k+}} \psi_j^*(r_k) e^{i(m_k - m_j)\theta} \right\} \delta(r - r_k), \quad (\text{A33})$$

$$\begin{aligned} \mathcal{J} (\mu_0 \delta \mathbf{J} \times \delta \mathbf{B})_\phi &= -\frac{R_0}{2} \sum_{k,j} \frac{n}{m_k} \\ &\times \text{Re} \left\{ i [\chi_k]_{r_{k-}}^{r_{k+}} \psi_j^*(r_k) e^{i(m_k - m_j)\theta} \right\} \delta(r - r_k), \end{aligned} \quad (\text{A34})$$

where use has been made of Eqs. (A14), (A29), and (A30). Let

$$\Psi_k = \frac{\psi_k(r_k)}{m_k}, \quad (\text{A35})$$

$$\Delta \Psi_k = [\chi_k]_{r_{k-}}^{r_{k+}}, \quad (\text{A36})$$

$$\delta T_{\theta k} = \int_{r_{k-}}^{r_{k+}} \oint \oint (\delta \mathbf{J} \times \delta \mathbf{B})_\theta \mathcal{J} dr d\theta d\phi, \quad (\text{A37})$$

$$\delta T_{\phi k} = \int_{r_{k-}}^{r_{k+}} \oint \oint (\delta \mathbf{J} \times \delta \mathbf{B})_\phi \mathcal{J} dr d\theta d\phi \quad (\text{A38})$$

for $k = 1, K$. It follows that^{25,29,34}

$$\delta T_{\theta k} = -\frac{2\pi^2 R_0}{\mu_0} m_k \text{Im}(\Psi_k^* \Delta \Psi_k), \quad (\text{A39})$$

$$\delta T_{\phi k} = \frac{2\pi^2 R_0}{\mu_0} n \text{Im}(\Psi_k^* \Delta \Psi_k). \quad (\text{A40})$$

Note that Ψ_k parameterizes the reconnected magnetic flux at the k th resonant surface, whereas $\Delta \Psi_k$ (which has the same units as Ψ_k) parameterizes the strength of the current sheet that forms at that surface.^{25,29} Furthermore, $\delta T_{\theta k}$ and $\delta T_{\phi k}$ are the net poloidal and toroidal electromagnetic torques, respectively, acting at the k th resonant surface.

6. Derivation of toroidal tearing mode dispersion relation

In principle, we could determine the relationship between the $\Delta \Psi_k$ and the Ψ_k by solving Eqs. (A16) and (A17) subject to suitable spatial boundary conditions at $r = 0$ and $r = a$.^{25,28,29} However, in this paper, we shall adopt a more direct approach.

We can write

$$\delta \mathbf{B} = \nabla \times \delta \mathbf{A}. \quad (\text{A41})$$

Suppose that $r \delta A_r$ and δA_θ are negligible with respect to δA_ϕ . In fact, it follows from $\nabla \cdot \delta \mathbf{A} = 0$ that $r \delta A_r, \delta A_\theta \sim (n/m)(r/R)^2 \delta A_\phi$. Hence

$$\mathcal{J} \delta B^r \simeq \frac{\partial \delta A_\phi}{\partial \theta}, \quad (\text{A42})$$

$$\mathcal{J} \delta B^\theta \simeq -\frac{\partial \delta A_\phi}{\partial r}, \quad (\text{A43})$$

$$\mathcal{J} \delta B^\phi \simeq 0, \quad (\text{A44})$$

where the neglected terms are of order $(n/m)^2 (r/R)^2$ smaller than the retained terms. The previous three expressions are consistent with Eqs. (A14), (A21), and (A22) provided that

$$\delta A_\phi(r, \theta, \phi) \simeq R_0 \sum_j \frac{\psi_j(r)}{m_j} e^{i(m_j \theta - n \phi)}. \quad (\text{A45})$$

According to the Biot-Savart law

$$\delta A_\phi(\mathbf{x}) = \frac{\mu_0}{4\pi} \int \frac{R R' \delta \mathbf{J}(\mathbf{x}') \cdot \nabla \phi}{|\mathbf{x} - \mathbf{x}'|} d^3 \mathbf{x}'. \quad (\text{A46})$$

Let us assume that

$$\delta A_\phi(R, \phi, Z) = \delta A_\phi(R, 0, Z) e^{-in\phi}. \quad (\text{A47})$$

It follows that we can evaluate the integral on the right-hand side of Eq. (A46) at $\phi = 0$ without loss of generality. Now

$$\delta \mathbf{J}(R', \phi', Z') \cdot \nabla \phi = \delta J^\phi(R', 0, Z') e^{-in\phi'} \cos \phi' \quad (\text{A48})$$

so we get

$$\delta A_\phi(R, 0, Z) = \frac{\mu_0}{4\pi} \int_0^\infty \oint R R' \delta J^\phi(R', 0, Z') G(R, Z; R', Z') \mathcal{J}' dr' d\theta', \quad (\text{A49})$$

where

$$G(R, Z; R', Z') = \frac{1}{2} \oint \frac{(\cos[(n-1)\phi'] + \cos[(n+1)\phi']) d\phi'}{[R^2 + R'^2 + (Z - Z')^2 - 2 R R' \cos \phi']^{1/2}}. \quad (\text{A50})$$

Finally, making use of the standard definition of a toroidal function⁵³

$$P_{-1/2}^n(\cosh \eta) = \frac{(-1)^n \Gamma(1/2) \Gamma(1/2 + n)}{2\pi^2} \oint \frac{\cos(n\varphi) d\varphi}{(\cosh \eta - \sinh \eta \cos \varphi)^{1/2}}, \quad (\text{A51})$$

we arrive at

$$G(R, Z; R', Z') = \frac{(-1)^{n+1} \pi^2}{\Gamma(1/2) \Gamma(n+1/2)} \left[\frac{\cosh \eta}{R^2 + R'^2 + (Z - Z')^2} \right]^{1/2} \times \left[(n-1/2) P_{-1/2}^{n-1}(\cosh \eta) + \frac{P_{-1/2}^{n+1}(\cosh \eta)}{n+1/2} \right], \quad (\text{A52})$$

where

$$\eta = \tanh^{-1} \left[\frac{2 R R'}{R^2 + R'^2 + (Z - Z')^2} \right]. \quad (\text{A53})$$

According to Eqs. (A30) and (A36)

$$\mathcal{J} \mu_0 \delta J^\phi(r, \theta, 0) = - \sum_{k=1, K} \Delta \Psi_k \delta(r - r_k) e^{im_k \theta}. \quad (\text{A54})$$

Furthermore, Eqs. (A35) and (A45) yield

$$\Psi_k = \frac{1}{R_0} \oint \delta A_\phi(r_k, \theta, 0) e^{-im_k \theta} \frac{d\theta}{2\pi}. \quad (\text{A55})$$

Hence, combining the previous two expression with Eq. (A49), we obtain the following toroidal tearing mode dispersion relation:^{25,29}

$$\Psi_k = \sum_{k'=1, K} F_{kk'} \Delta \Psi_{k'} \quad (\text{A56})$$

for $k = 1, K$, where

$$F_{kk'} = \oint \oint \mathcal{G}(R_k, Z_k; R_{k'}, Z_{k'}) e^{-i(m_k \theta_k - m_{k'} \theta_{k'})} \frac{d\theta_k}{2\pi} \frac{d\theta_{k'}}{2\pi} \quad (\text{A57})$$

and

$$\mathcal{G}(R_k, Z_k; R_{k'}, Z_{k'}) = \frac{(-1)^n \pi^2 R_k R_{k'} / R_0}{2\Gamma(1/2) \Gamma(n+1/2)} \left[\frac{\cosh \eta_{kk'}}{R_k^2 + R_{k'}^2 + (Z_k - Z_{k'})^2} \right]^{1/2} \times \left[(n-1/2) P_{-1/2}^{n-1}(\cosh \eta_{kk'}) + \frac{P_{-1/2}^{n+1}(\cosh \eta_{kk'})}{n+1/2} \right] \quad (\text{A58})$$

with

$$\eta_{kk'} = \tanh^{-1} \left[\frac{2 R_k R_{k'}}{R_k^2 + R_{k'}^2 + (Z_k - Z_{k'})^2} \right]. \quad (\text{A59})$$

Here, k and k' index the various resonant surfaces in the plasma. Moreover, the double integral in Eq. (A57) is taken around the k th resonant surface (cylindrical coordinates $R_k, 0, Z_k$; flux coordinates $r_k, \theta_k, 0$, with r_k constant; resonant poloidal mode number m_k) and the k' th resonant surface (cylindrical coordinates $R_{k'}, 0, Z_{k'}$; flux coordinates $r_{k'}, \theta_{k'}, 0$, with $r_{k'}$ constant; resonant poloidal mode number $m_{k'}$).

Note that

$$\mathcal{G}(R_{k'}, Z_{k'}; R_k, Z_k) = \mathcal{G}(R_k, Z_k; R_{k'}, Z_{k'}) \quad (\text{A60})$$

which, from Eq. (A57), implies that

$$F_{k'k} = F_{kk'}^*. \quad (\text{A61})$$

Hence, Eqs. (A39) and (A40) yield^{25,29,34}

$$\sum_{k=1, K} \delta T_{\theta k} = \sum_{k=1, K} \delta T_{\phi k} = 0. \quad (\text{A62})$$

In other words, we deduce that the plasma cannot exert a net electromagnetic torque on itself.

The toroidal tearing mode dispersion relation is more usually written^{25,29}

$$\Delta \Psi_k = \sum_{k'=1, K} E_{kk'} \Psi_{k'} \quad (\text{A63})$$

for $k = 1, K$, where the Hermitian matrix $E_{kk'}$ is the inverse of the $F_{kk'}$ matrix. The real quantity E_{kk} represents the standard tearing stability index²⁴ (normalized to the minor radius of the resonant surface) for a tearing mode that only reconnects magnetic flux at the k th resonant surface.²⁵ Given that there are no sources of plasma free energy in our tearing response model, we expect all of the E_{kk} to be negative. In other words, we expect the plasma to be tearing stable.

7. Effect of external currents

Suppose that there are currents flowing in a number of poloidal magnetic field coils external to the plasma. We can represent these currents as a set of toroidal current filaments. The currents in the various filaments are assumed to modulate toroidally as $e^{-in\phi}$. It follows that

$$\delta J_{\text{ext}}^{\phi}(R, 0, Z) = \sum_{l=1,L} \frac{I_l}{R_l} \delta(R - R_l) \delta(Z - Z_l), \quad (\text{A64})$$

where R_l and Z_l are the coordinates of the l th current filament in the $\phi = 0$ plane, and I_l is the complex amplitude of the toroidal current flowing in the filament. Here, it is assumed that there are L current filaments, numbered 1 to L . Under normal circumstances, we would expect zero net toroidal current to flow in the external field coils. In other words,

$$\sum_{l=1,L} I_l = 0. \quad (\text{A65})$$

In the presence of the external currents, it is easily demonstrated that the toroidal tearing mode dispersion relation Eq. (A56) generalizes to give

$$\Psi_k = \sum_{k'=1,K} F_{kk'} \Delta \Psi_{k'} - \sum_{l=1,L} g_{kl} \mu_0 I_l \quad (\text{A66})$$

for $k = 1, K$ and $l = 1, L$, where

$$g_{kl} = \frac{1}{2\pi} \oint \mathcal{G}(R_k, Z_k; R_l, Z_l) e^{-im_k \theta_k} \frac{d\theta_k}{2\pi}. \quad (\text{A67})$$

Here, k indexes the various resonant surfaces in the plasma, whereas l indexes the external current filaments. Moreover, the integral in Eq. (A67) is taken around the k th resonant surface (cylindrical coordinates $R_k, 0, Z_k$; flux coordinates $r_k, \theta_k, 0$, with r_k constant; resonant poloidal mode number m_k).

It is convenient to rewrite Eq. (A66) in the form

$$\Delta \Psi_k = \sum_{k'=1,K} E_{kk'} \Psi_{k'} + |E_{kk}| \chi_k, \quad (\text{A68})$$

where

$$\chi_k = \frac{1}{|E_{kk}|} \sum_{l=1,L} h_{kl} \mu_0 I_l \quad (\text{A69})$$

and

$$h_{kl} = \sum_{k'=1,K} E_{kk'} g_{k'l}. \quad (\text{A70})$$

The quantity χ_k that appears in Eq. (A68) is the reconnected magnetic flux driven at the k th resonant surface by the external currents when there is no shielding of driven magnetic reconnection at the surface in question (i.e., $\Delta \Psi_k = 0$), but perfect shielding at all of the other resonant surfaces (i.e., $\Psi_{k' \neq k} = 0$).

8. Model of kink response of plasma

If we define the equilibrium toroidal flux, $\Psi_t(r)$, such that

$$\frac{d\Psi_t}{dr} = q(r) \frac{d\Psi_p}{dr} = 2\pi B_0 r g(r), \quad (\text{A71})$$

then the equilibrium magnetic field can be written in the form [see Eqs. (A1)–(A4)]⁵⁴

$$2\pi \mathbf{B} = q^{-1} \nabla \phi \times \nabla \Psi_t + \nabla \Psi_t \times \nabla \theta. \quad (\text{A72})$$

Moreover, the current sheets that develop at the various resonant surfaces in the plasma are specified by [see Eqs. (A28)–(A30) and (A36)]^{54,55}

$$\mu_0 \delta \mathbf{J} = -2\pi \sum_{k=1,K} \Delta \Psi_k e^{i(m_k \theta - n \phi)} \delta(\Psi_t - \Psi_{tk}) \mathbf{B}, \quad (\text{A73})$$

where Ψ_{tk} is the equilibrium toroidal flux enclosed by the k th resonant surface. Let [see Eqs. (A14) and (A16)]^{54,55}

$$\begin{aligned} \Delta_k e^{i(m_k \theta - n \phi)} &= \left[\frac{\partial}{\partial r} \frac{\delta B^r}{\mathbf{B} \cdot \nabla \phi} \right]_{r_{k-}}^{r_{k+}} \\ &= i \left(\frac{R_0}{r_k} \right)^2 \frac{1}{B_0 R_0 g(r_k)} \left[r \frac{d\psi_k}{dr} \right]_{r_{k-}}^{r_{k+}} e^{i(m_k \theta - n \phi)}. \end{aligned} \quad (\text{A74})$$

It follows that [see Eqs. (A16) and (A36)]

$$\Delta_k = i \left(\frac{R_0}{r_k} \right)^2 \frac{m_k a_{kk}(r_k)}{g(r_k)} \frac{\Delta \Psi_k}{B_0 R_0}. \quad (\text{A75})$$

Note that Eqs. (A73) and (A75) are entirely equivalent to Eqs. (2) and (3) in Ref. 55, and Eqs. (44)–(46), (51) and (53) in Ref. 54 [in the limit that $(n/m)^2 (r/R)^2 \ll 1$]. This observation gives added confidence that the analysis contained in this Appendix is essentially correct.

It turns out that the GPEC code³³ is capable of calculating the Δ_k values when a plasma equilibrium responds ideally to a given externally generated RMP. For the ideal case (i.e., $\Psi_k = 0$ for all k), we have $\Delta \Psi_k = |E_{kk}| \chi_k$ [see Eq. (A68)]. Hence, the χ_k values, which epitomize the kink response of the plasma to the applied RMP, can be calculated from the GPEC Δ_k values, as follows:

$$\frac{\chi_k}{B_0 R_0} = -i \left(\frac{r_k}{R_0} \right)^2 \frac{g(r_k)}{m_k a_{kk}(r_k)} \frac{\Delta_k}{|E_{kk}|}. \quad (\text{A76})$$

9. Heuristic model of kink response of plasma

As an alternative (and far simpler, but much less accurate) method of incorporating the kink response of the plasma to the applied RMP into our model, we introduce a control surface, labeled $K+1$, on the plasma boundary. This surface is presumed to act like a resonant surface whose poloidal mode number is

$m_{K+1} = m_K + 1$. By analogy with our previous analysis, we can write

$$\Delta\Psi_k = \sum_{k'=1,K} E_{kk'} \Psi_{k'} + E_{k,K+1} \Psi_{K+1} + \sum_{l=1,L} h_{kl} \mu_0 I_l \quad (\text{A77})$$

for $k = 1, K$. The ideal (i.e., $\Psi_k = 0$, for $k = 1, K$) response of the control surface is governed by

$$\Delta\Psi_{K+1} = E_{K+1,K+1} \Psi_{K+1} + \sum_{l=1,L} h_{K+1,l} \mu_0 I_l. \quad (\text{A78})$$

Let us replace $E_{K+1,K+1}$ by $-s_{\text{kink}}$, where s_{kink} is a dimensionless adjustable parameter. We expect there to be no shielding current at the control surface (i.e., $\Delta\Psi_{K+1} = 0$). Hence, we can combine the previous two equations to obtain the modified toroidal tearing mode dispersion relation,

$$\Delta\Psi_k = \sum_{k'=1,K} E_{kk'} \Psi_{k'} + |E_{kk}| \chi_k \quad (\text{A79})$$

for $k = 1, K$, where

$$\chi_k = \frac{1}{|E_{kk}|} \sum_{l=1,L} \left(h_{kl} + \frac{E_{k,K+1} h_{K+1,l}}{s_{\text{kink}}} \right) \mu_0 I_l. \quad (\text{A80})$$

We interpret Eq. (A79) as implying that the ideal response of the plasma to the applied RMP has the effect of amplifying the RMP via coupling to a stable non-resonant kink mode. The stability of the kink mode is governed by the parameter s_{kink} . The mode is extremely stable in the limit $s_{\text{kink}} \rightarrow \infty$ (in which case there is no amplification), and approaches marginal stability as $s_{\text{kink}} \rightarrow 0$ (in which case the amplification becomes very strong).

10. Perturbed poloidal magnetic field

The perturbed poloidal magnetic field generated by the current sheets inside the plasma and the currents flowing in the external field coils can be expressed as

$$\delta\mathbf{B}_p = \nabla\delta A_\phi \times \nabla\phi, \quad (\text{A81})$$

where

$$\frac{\delta A_\phi(R, \phi, Z)}{R_0} = \text{Re} \left[\sum_{k=1,K} e_k(R, Z) \Delta\Psi_k e^{-in\phi} - \sum_{l=1,L} f_l(R, Z) \mu_0 I_l e^{-in\phi} \right] \quad (\text{A82})$$

and

$$e_k(R, Z) = \oint \mathcal{G}(R, Z; R_k; Z_k) e^{im_k\theta_k} \frac{d\theta_k}{2\pi}, \quad (\text{A83})$$

$$f_l(R, Z) = \frac{1}{2\pi} \mathcal{G}(R, Z; R_l; Z_l). \quad (\text{A84})$$

As before, k indexes the resonant surfaces within the plasma, whereas l indexes the external current filaments. Moreover, the integral in Eq. (A83) is taken around the k th resonant surface (cylindrical coordinates $R_k, 0, Z_k$; flux coordinates $r_k, \theta_k, 0$, with r_k constant; resonant poloidal mode number m_k).

11. Electromagnetic torques in presence of external currents

Suppose that

$$\Psi_k = B_0 R_0 \hat{\Psi}_k e^{-i\varphi_k}, \quad (\text{A85})$$

$$\chi_k = B_0 R_0 \hat{\chi}_k e^{-i\zeta_k}, \quad (\text{A86})$$

$$E_{kk'} = \hat{E}_{kk'} e^{-i\zeta_{kk'}}, \quad (\text{A87})$$

where $\hat{\Psi}_k$, $\hat{\chi}_k$, and $\hat{E}_{kk'}$ are real and positive, whereas φ_k , ζ_k , and $\zeta_{kk'}$ are real. (Note that all hatted quantities in this paper are dimensionless.) It follows from Eqs. (A39), (A40), and (A68) that

$$\delta T_{\theta k} = - \left(\frac{2\pi^2 B_0^2 R_0^3}{\mu_0} \right) m_k \delta \hat{T}_k, \quad (\text{A88})$$

$$\delta T_{\phi k} = \left(\frac{2\pi^2 B_0^2 R_0^3}{\mu_0} \right) n \delta \hat{T}_k, \quad (\text{A89})$$

where

$$\begin{aligned} \delta \hat{T}_k &= \sum_{k'=1,K} \hat{E}_{kk'} \hat{\Psi}_k \hat{\Psi}_{k'} \sin(\varphi_k - \varphi_{k'} - \zeta_{kk'}) \\ &+ \hat{E}_{kk} \hat{\Psi}_k \hat{\chi}_k \sin(\varphi_k - \zeta_k). \end{aligned} \quad (\text{A90})$$

APPENDIX B: NEOCLASSICAL PHYSICS

1. Plasma species

The plasma is assumed to consist of three (charged) species; namely, electrons (e), majority ions (i), and impurity ions (I). The charges of the three species are $e_e = -e$, $e_i = e$, and $e_I = Z_I e$, respectively, where e is the magnitude of the electron charge. The mean impurity ion charge number, $Z_I(r)$, for a given impurity species is determined as a function of the electron temperature and density using data obtained from the FLYCHK code.³⁹ Quasineutrality demands that $n_e = n_i + Z_I n_I$, where $n_a(r)$ is the species- a number density. Let

$$\alpha_I(r) = \frac{Z_I (Z_{\text{eff}} - 1)}{Z_I - Z_{\text{eff}}}, \quad (\text{B1})$$

where

$$Z_{\text{eff}}(r) = \frac{n_i + Z_I^2 n_I}{n_e} \quad (\text{B2})$$

is the effective ion charge number. It follows that

$$\frac{n_i}{n_e} = \frac{Z_I - Z_{\text{eff}}}{Z_I - 1}, \quad (\text{B3})$$

$$\frac{n_I}{n_e} = \frac{Z_{\text{eff}} - 1}{Z_I (Z_I - 1)}. \quad (\text{B4})$$

2. Collisionality parameters

Consider an equilibrium magnetic flux-surface whose label is r . Let

$$\frac{1}{\gamma(r)} = \frac{q}{g} \oint \frac{B R^2}{B_0 R_0^2} \frac{d\theta}{2\pi}, \quad (\text{B5})$$

where $B = |\mathbf{B}|$. It is helpful to define a new poloidal angle Θ such that

$$\frac{d\Theta}{d\theta} = \frac{\gamma q}{g} \frac{B R^2}{B_0 R_0^2}. \quad (\text{B6})$$

Let

$$I_1 = \oint \frac{B_0}{B} \frac{d\Theta}{2\pi}, \quad (\text{B7})$$

$$I_2 = \oint \frac{B}{B_0} \frac{d\Theta}{2\pi}, \quad (\text{B8})$$

$$I_3 = \oint \left(\frac{\partial B}{\partial \Theta} \right)^2 \frac{1}{B_0 B} \frac{d\Theta}{2\pi}, \quad (\text{B9})$$

$$I_{4,c} = \sqrt{2} c \oint \frac{\cos(c\Theta)}{B/B_0} \frac{d\Theta}{2\pi}, \quad (\text{B10})$$

$$I_{5,c} = \sqrt{2} c \oint \frac{\cos(c\Theta)}{2(B/B_0)^2} \frac{d\Theta}{2\pi}, \quad (\text{B11})$$

$$I_6(\lambda) = \oint \frac{\sqrt{1 - \lambda B/B_{\max}}}{B/B_0} \frac{d\Theta}{2\pi}, \quad (\text{B12})$$

where B_{\max} is the maximum value of B on the magnetic flux-surface, and c a positive integer. The species- a transit frequency is written³⁸

$$\omega_{ta}(r) = K_t \gamma v_{Ta}, \quad (\text{B13})$$

where

$$K_t(r) = \frac{I_1^2 I_3}{I_2^2 \sum_{c=1,C} I_{4,c} I_{5,c}}, \quad (\text{B14})$$

$C \gg 1$, and $v_{Ta} = \sqrt{2 T_a/m_a}$. Here, m_a is the species- a mass, and $T_a(r)$ the species a temperature (in energy units). The fraction of circulating particles is³⁸

$$f_c(r) = \frac{3 I_2}{4} \frac{B_0^2}{B_{\max}^2} \int_0^1 \frac{\lambda d\lambda}{I_6(\lambda)}. \quad (\text{B15})$$

Finally, the dimensionless species- a collisionality parameter is written³⁸

$$\nu_{*a}(r) = K_* \frac{g_t}{\omega_{ta} \tau_{aa}}, \quad (\text{B16})$$

where

$$g_t(r) = \frac{f_c}{1 - f_c}, \quad (\text{B17})$$

$$K_*(r) = \frac{3}{8\pi} \frac{I_2}{I_3} K_t^2, \quad (\text{B18})$$

$$\frac{1}{\tau_{aa}} = \frac{4}{3\sqrt{\pi}} \frac{4\pi n_a e_a^4 \ln \Lambda}{(4\pi \epsilon_0)^2 m_a^2 v_{Ta}^3}. \quad (\text{B19})$$

Here, the Coulomb logarithm, $\ln \Lambda$, is assumed to take the same large constant value (i.e., $\ln \Lambda \simeq 17$), independent of species.

3. Ion collisional friction matrices

Let $x_{ab} = v_{Tb}/v_{Ta}$. In the following, all quantities that are of order $(m_e/m_i)^{1/2}$, $(m_e/m_i)^{1/2}$, or smaller, are neglected with respect to unity. The 2×2 dimensionless ion collisional friction matrices, $[F^{ii}](r)$, $[F^{il}](r)$, $[F^{li}](r)$, and $[F^{ll}](r)$, are defined to have the following elements:^{37,38}

$$F_{00}^{ii} = \frac{\alpha_i (1 + m_i/m_l)}{(1 + x_{il}^2)^{3/2}}, \quad (\text{B20})$$

$$F_{01}^{ii} = \frac{3}{2} \frac{\alpha_i (1 + m_i/m_l)}{(1 + x_{il}^2)^{5/2}}, \quad (\text{B21})$$

$$F_{10}^{ii} = F_{01}^{ii}, \quad (\text{B22})$$

$$F_{11}^{ii} = \sqrt{2} + \frac{\alpha_i [13/4 + 4x_{il}^2 + (15/2)x_{il}^4]}{(1 + x_{il}^2)^{5/2}}, \quad (\text{B23})$$

$$F_{00}^{il} = F_{00}^{ii}, \quad (\text{B24})$$

$$F_{01}^{il} = \frac{3}{2} \frac{T_i}{T_l} \frac{\alpha_i (1 + m_l/m_i)}{x_{il} (1 + x_{il}^2)^{5/2}}, \quad (\text{B25})$$

$$F_{10}^{il} = F_{01}^{il}, \quad (\text{B26})$$

$$F_{11}^{il} = \frac{27}{4} \frac{T_i}{T_l} \frac{\alpha_i x_{il}^2}{(1 + x_{il}^2)^{5/2}}, \quad (\text{B27})$$

$$F_{00}^{li} = F_{00}^{ii}, \quad (\text{B28})$$

$$F_{01}^{li} = F_{01}^{ii}, \quad (\text{B29})$$

$$F_{10}^{li} = F_{01}^{li}, \quad (\text{B30})$$

$$F_{11}^{li} = \frac{27}{4} \frac{\alpha_i x_{il}^2}{(1 + x_{il}^2)^{5/2}}, \quad (\text{B31})$$

$$F_{00}^{ll} = F_{00}^{ii}, \quad (\text{B32})$$

$$F_{01}^{ll} = F_{01}^{ii}, \quad (\text{B33})$$

$$F_{10}^{ll} = F_{01}^{ll}, \quad (\text{B34})$$

$$F_{11}^{ll} = \frac{T_i}{T_l} \left\{ \sqrt{2} \alpha_i^2 x_{li} + \frac{\alpha_i [15/2 + 4x_{il}^2 + (13/4)x_{il}^4]}{(1 + x_{il}^2)^{5/2}} \right\}. \quad (\text{B35})$$

4. Electron collisional friction matrix

The 2×2 dimensionless electron collisional friction matrix, $[F^{ee}](r)$, is defined to have the following elements:³⁸

$$F_{00}^{ee} = Z_{\text{eff}}, \quad (\text{B36})$$

$$F_{01}^{ee} = \frac{3}{2} Z_{\text{eff}}, \quad (\text{B37})$$

$$F_{10}^{ee} = \frac{3}{2} Z_{\text{eff}}, \quad (\text{B38})$$

$$F_{11}^{ee} = \sqrt{2} + \frac{13}{4} Z_{\text{eff}}. \quad (\text{B39})$$

5. Neoclassical viscosity matrices

The 2×2 dimensionless species- a neoclassical viscosity matrix, $[\mu^a](r)$, is defined to have the following elements:³⁸

$$\mu_{00}^a = K_{00}^a, \quad (\text{B40})$$

$$\mu_{01}^a = \frac{5}{2} K_{00}^a - K_{01}^a, \quad (\text{B41})$$

$$\mu_{10}^a = \mu_{01}^a, \quad (\text{B42})$$

$$\mu_{11}^a = K_{11}^a - 5 K_{01}^a + \frac{25}{4} K_{00}^a. \quad (\text{B43})$$

Here

$$K_{ab}^e = g_t \frac{4}{3\sqrt{\pi}} \int_0^\infty \frac{e^{-x} x^{4+a+b} \nu_D^e(x) dx}{[x^2 + \nu_{*e} \nu_D^e(x)] [x^2 + (5\pi/8) (\omega_{te} \tau_{ee})^{-1} \nu_T^e(x)]}, \quad (\text{B44})$$

$$\nu_D^e = \frac{3\sqrt{\pi}}{4} \left[\left(1 - \frac{1}{2x}\right) \psi(x) + \psi'(x) \right] + \frac{3\sqrt{\pi}}{4} Z_{\text{eff}}, \quad (\text{B45})$$

$$\nu_e^e = \frac{3\sqrt{\pi}}{2} [\psi(x) - \psi'(x)], \quad (\text{B46})$$

$$\nu_T^e(x) = 3 \nu_D^e(x) + \nu_e^e(x) \quad (\text{B47})$$

and

$$\psi(x) = \frac{2}{\sqrt{\pi}} \int_0^x e^{-t^2} dt - \frac{2}{\sqrt{\pi}} x e^{-x^2}, \quad (\text{B48})$$

$$\psi'(x) = \frac{2}{\sqrt{\pi}} x e^{-x^2}. \quad (\text{B49})$$

Furthermore

$$K_{ab}^i = g_t \frac{4}{3\sqrt{\pi}} \int_0^\infty \frac{e^{-x} x^{2+a+b} \nu_D^i(x) dx}{[x + \nu_{*i} \nu_D^i(x)] [x + (5\pi/8) (\omega_{ti} \tau_{ii})^{-1} \nu_T^i(x)]}, \quad (\text{B50})$$

$$\nu_D^i = \frac{3\sqrt{\pi}}{4} \left[\left(1 - \frac{1}{2x}\right) \psi(x) + \psi'(x) \right] \frac{1}{x} + \frac{3\sqrt{\pi}}{4} \alpha_I \left[\left(1 - \frac{x_{ii}}{2x}\right) \psi\left(\frac{x}{x_{ii}}\right) + \psi'\left(\frac{x}{x_{ii}}\right) \right] \frac{1}{x}, \quad (\text{B51})$$

$$\nu_e^i = \frac{3\sqrt{\pi}}{2} [\psi(x) - \psi'(x)] \frac{1}{x} + \frac{3\sqrt{\pi}}{2} \alpha_I \left[\frac{m_i}{m_I} \psi\left(\frac{x}{x_{ii}}\right) - \psi'\left(\frac{x}{x_{ii}}\right) \right] \frac{1}{x}, \quad (\text{B52})$$

$$\nu_T^i(x) = 3 \nu_D^i(x) + \nu_e^i(x)$$

and, finally

$$K_{ab}^I = g_t \frac{4}{3\sqrt{\pi}} \int_0^\infty \frac{e^{-x} x^{2+a+b} \nu_D^I(x) dx}{[x + \nu_{*I} \nu_D^I(x)] [x + (5\pi/8) (\omega_{tI} \tau_{II})^{-1} \nu_T^I(x)]}, \quad (\text{B53})$$

$$\nu_D^I = \frac{3\sqrt{\pi}}{4} \left[\left(1 - \frac{1}{2x}\right) \psi(x) + \psi'(x) \right] \frac{1}{x} + \frac{3\sqrt{\pi}}{4} \frac{1}{\alpha_I} \left[\left(1 - \frac{x_{II}}{2x}\right) \psi\left(\frac{x}{x_{II}}\right) + \psi'\left(\frac{x}{x_{II}}\right) \right] \frac{1}{x}, \quad (\text{B54})$$

$$\nu_e^I = \frac{3\sqrt{\pi}}{2} [\psi(x) - \psi'(x)] \frac{1}{x} + \frac{3\sqrt{\pi}}{2} \frac{1}{\alpha_I} \left[\frac{m_I}{m_i} \psi\left(\frac{x}{x_{II}}\right) - \psi'\left(\frac{x}{x_{II}}\right) \right] \frac{1}{x}, \quad (\text{B55})$$

$$\nu_T^I(x) = 3 \nu_D^I(x) + \nu_e^I(x). \quad (\text{B56})$$

Note that our expressions for the neoclassical viscosity matrices interpolate in the most accurate manner possible between the three standard neoclassical collisionality regimes (i.e., the banana, plateau, and Pfirsch-Schütter regimes).³⁸

6. Parallel force and heat balance

Let

$$[\tilde{\mu}^I] = \alpha_T^2 \frac{T_i}{T_I} x_{II} [\mu^I]. \quad (\text{B57})$$

The requirement of equilibrium force and heat balance parallel to the magnetic field^{37,38,41} leads us to define four 2×2 dimensionless ion matrices, $[L^{ii}](r)$, $[L^{II}](r)$, $[L^{ii}](r)$, and $[L^{II}](r)$, where

$$\begin{pmatrix} [L^{ii}], & [L^{II}] \\ [L^{ii}], & [L^{II}] \end{pmatrix} = \begin{pmatrix} [F^{ii} + \mu^i + Y^{in}/y_n], & -[F^{iI}] \\ -[F^{ii}], & [F^{II} + \tilde{\mu}^I] \end{pmatrix}^{-1} \times \begin{pmatrix} [F^{ii} + Y^{in}], & -[F^{iI}] \\ -[F^{ii}], & [F^{II}] \end{pmatrix} \quad (\text{B58})$$

and the 2×2 dimensionless electron matrix, $[Q^{ee}](r)$, where

$$[Q^{ee}] = [F^{ee} + \mu^e]^{-1}. \quad (\text{B59})$$

Here,⁴¹

$$[Y^{in}] = \tau_{ii} \langle \sigma v \rangle_i^{\text{cx}} \langle n_n \rangle \begin{bmatrix} 1, & 0 \\ 0, & E_n/T_i \end{bmatrix}, \quad (\text{B60})$$

$$y_n = \frac{\langle n_n \rangle \langle B^2 \rangle}{\langle n_n B^2 \rangle}, \quad (\text{B61})$$

where

$$\langle A \rangle(r) \equiv \oint \frac{A(r, \Theta) d\Theta}{B(r, \Theta)} \bigg/ \oint \frac{d\Theta}{B(r, \Theta)}. \quad (\text{B62})$$

Moreover, $\langle \sigma v \rangle_i^{\text{cx}}$ is the flux-surface averaged rate constant for charge exchange reactions between neutrals and majority ions, $n_n(r, \Theta)$ the neutral particle density, and E_n/T_i the ratio of the incoming neutral energy to the majority ion energy. The parameter y_n takes into account the fact that the incoming neutrals at the edge of an H-mode tokamak plasma are usually concentrated at the X-point (i.e., $y_n > 1$).⁴¹

APPENDIX C: PLASMA ANGULAR VELOCITY EVOLUTION

1. Plasma angular equations of motion

We can write

$$\Omega_\theta(r, t) = \Omega_{\theta 0}(r) + \Delta \Omega_\theta(r, t), \quad (\text{C1})$$

$$\Omega_\phi(r, t) = \Omega_{\phi 0}(r) + \Delta \Omega_\phi(r, t), \quad (\text{C2})$$

where $\Omega_\theta(r, t)$ and $\Omega_\phi(r, t)$ are the poloidal and toroidal plasma angular velocity profiles, respectively, whereas $\Omega_{\theta 0}(r)$ and $\Omega_{\phi 0}(r)$

are the corresponding unperturbed profiles, and $\Delta\Omega_\theta(r, t)$ and $\Delta\Omega_\phi(r, t)$ are the respective modifications to the profiles induced by the electromagnetic torques exerted at the various resonant surfaces within the plasma. The modifications to the angular velocity profiles are governed by the poloidal and toroidal angular equations of motion of the plasma, which take the respective forms^{34,56}

$$4\pi^2 R_0 \left[(1 + 2q^2) \rho r^3 \frac{\partial \Delta\Omega_\theta}{\partial t} - \frac{\partial}{\partial r} \left(\mu r^3 \frac{\partial \Delta\Omega_\theta}{\partial r} \right) + \frac{\rho}{\tau_\theta} r^3 \Delta\Omega_\theta \right] = \sum_{k=1, K} \delta T_{\theta k} \delta(r - r_k), \quad (C3)$$

$$4\pi^2 R_0^3 \left[\rho r \frac{\partial \Delta\Omega_\phi}{\partial t} - \frac{\partial}{\partial r} \left(\mu r \frac{\partial \Delta\Omega_\phi}{\partial r} \right) + \frac{\rho}{\tau_\phi} r \Delta\Omega_\phi \right] = \sum_{k=1, K} \delta T_{\phi k} \delta(r - r_k) \quad (C4)$$

and are subject to the spatial boundary conditions³⁴

$$\frac{\partial \Delta\Omega_\theta(0, t)}{\partial r} = \frac{\partial \Delta\Omega_\phi(0, t)}{\partial r} = 0, \quad (C5)$$

$$\Delta\Omega_\theta(a, t) = \Delta\Omega_\phi(a, t) = 0. \quad (C6)$$

Here, $\mu(r)$ is the anomalous plasma perpendicular ion viscosity (due to plasma turbulence), whereas $\rho(r)$ is the plasma mass density profile. Furthermore, $1/\tau_\theta(r)$ is the neoclassical poloidal flow-damping rate.^{37,57} Finally, $1/\tau_\phi(r)$ is the neoclassical toroidal flow-damping rate.^{58,59} Note that Eqs. (C3) and (C4) are obtained by taking flux-surface averages of the poloidal and toroidal components of the plasma equation of motion. The flux-surface averaging annihilates the dominant scalar pressure and poloidally and toroidally varying $\mathbf{j} \times \mathbf{B}$ terms, leaving intact the much smaller inertial and viscous terms, as well as the residual net electromagnetic torques acting at the resonant surfaces.

According to standard neoclassical theory^{37,38}

$$\frac{1}{\tau_{ii}(r)} = \left(\frac{q R_0}{r} \right)^2 \frac{\mu_{00}^i}{\tau_{ii}}, \quad (C7)$$

where $\tau_{ii}(r)$ and $\mu_{00}^i(r)$ are defined in Appendix B.

2. Simplified plasma angular equations of motion

It is convenient to write

$$\Delta\Omega_\theta(r, t) = \sum_{k=1, K} \Delta\Omega_{\theta k}(r, t), \quad (C8)$$

$$\Delta\Omega_\phi(r, t) = \sum_{k=1, K} \Delta\Omega_{\phi k}(r, t), \quad (C9)$$

where

$$4\pi^2 R_0 \left[(1 + 2q^2) \rho r^3 \frac{\partial \Delta\Omega_{\theta k}}{\partial t} - \frac{\partial}{\partial r} \left(\mu r^3 \frac{\partial \Delta\Omega_{\theta k}}{\partial r} \right) + \frac{\rho}{\tau_\theta} r^3 \Delta\Omega_{\theta k} \right] = \delta T_{\theta k} \delta(r - r_k), \quad (C10)$$

$$4\pi^2 R_0^3 \left[\rho r \frac{\partial \Delta\Omega_{\phi k}}{\partial t} - \frac{\partial}{\partial r} \left(\mu r \frac{\partial \Delta\Omega_{\phi k}}{\partial r} \right) + \frac{\rho}{\tau_\phi} r \Delta\Omega_{\phi k} \right] = \delta T_{\phi k} \delta(r - r_k) \quad (C11)$$

and

$$\frac{\partial \Delta\Omega_{\theta k}(0, t)}{\partial r} = \frac{\partial \Delta\Omega_{\phi k}(0, t)}{\partial r} = 0, \quad (C12)$$

$$\Delta\Omega_{\theta k}(a, t) = \Delta\Omega_{\phi k}(a, t) = 0. \quad (C13)$$

Now, in the presence of poloidal and toroidal flow damping, the modified angular velocity profiles, $\Delta\Omega_{\theta k}$ and $\Delta\Omega_{\phi k}$, are radially localized in the vicinity of the k th resonant surface.⁵⁹ Hence, it is a good approximation to write Eqs. (C10) and (C11) in the simplified forms

$$4\pi^2 R_0 \left[(1 + 2q_k^2) \rho_k r^3 \frac{\partial \Delta\Omega_{\theta k}}{\partial t} - \mu_k \frac{\partial}{\partial r} \left(r^3 \frac{\partial \Delta\Omega_{\theta k}}{\partial r} \right) + \frac{\rho_k}{\tau_{\theta k}} r^3 \Delta\Omega_{\theta k} \right] = \delta T_{\theta k} \delta(r - r_k), \quad (C14)$$

$$4\pi^2 R_0^3 \left[\rho_k r \frac{\partial \Delta\Omega_{\phi k}}{\partial t} - \mu_k \frac{\partial}{\partial r} \left(r \frac{\partial \Delta\Omega_{\phi k}}{\partial r} \right) + \frac{\rho_k}{\tau_{\phi k}} r \Delta\Omega_{\phi k} \right] = \delta T_{\phi k} \delta(r - r_k), \quad (C15)$$

where $q_k = q(r_k)$, $\rho_k = \rho(r_k)$, $\mu_k = \mu(r_k)$, $\tau_{\theta k} = \tau_\theta(r_k)$, and $\tau_{\phi k} = \tau_\phi(r_k)$.

3. Normalized plasma equations of angular motion

Let

$$\tau_A = \left(\frac{\mu_0 \rho_0 a^2}{B_0^2} \right)^{1/2}, \quad (C16)$$

where $\rho_0 = \rho(0)$, and

$$\rho(r) = \left\{ m_i \left(\frac{Z_I - Z_{\text{eff}}}{Z_I - 1} \right) + m_I \left[\frac{Z_{\text{eff}} - 1}{Z_I (Z_I - 1)} \right] \right\} n_e \quad (C17)$$

is the plasma mass density. Furthermore, let $\hat{r} = r/a$, $\hat{r}_k = r_k/a$, $\hat{a} = a/R_0$, $\hat{t} = t/\tau_A$, $\hat{\rho}_k = \rho_k/\rho_0$, $\tau_{Mk} = \rho_k a^2/\mu_k$, $\hat{\tau}_{Mk} = \tau_{Mk}/\tau_A$, $\hat{\tau}_{\theta k} = \tau_{\theta k}/\tau_A$, $\hat{\tau}_{\phi k} = \tau_{\phi k}/\tau_A$, $\hat{\Omega}_\theta = \tau_A \Omega_\theta$, $\hat{\Omega}_{\theta 0} = \tau_A \Omega_{\theta 0}$, $\hat{\Delta\Omega}_{\theta k} = \tau_A \Delta\Omega_{\theta k}$, $\hat{\Omega}_\phi = \tau_A \Omega_\phi$, $\hat{\Omega}_{\phi 0} = \tau_A \Omega_{\phi 0}$, and $\hat{\Delta\Omega}_{\phi k} = \tau_A \Delta\Omega_{\phi k}$. It follows that

$$\hat{\Omega}_\theta(\hat{r}, \hat{t}) = \hat{\Omega}_{\theta 0}(\hat{r}) + \sum_{k=1, K} \hat{\Delta\Omega}_{\theta k}(\hat{r}, \hat{t}), \quad (C18)$$

$$\hat{\Omega}_\phi(\hat{r}, \hat{t}) = \hat{\Omega}_{\phi 0}(\hat{r}) + \sum_{k=1, K} \hat{\Delta\Omega}_{\phi k}(\hat{r}, \hat{t}), \quad (C19)$$

where

$$(1 + 2q_k^2) \hat{r}^3 \frac{\partial \hat{\Delta\Omega}_{\theta k}}{\partial \hat{t}} - \frac{1}{\hat{\tau}_{Mk}} \frac{\partial}{\partial \hat{r}} \left(\hat{r}^3 \frac{\partial \hat{\Delta\Omega}_{\theta k}}{\partial \hat{r}} \right) + \frac{1}{\hat{\tau}_{\theta k}} \hat{r}^3 \hat{\Delta\Omega}_{\theta k} = -\frac{m_k}{2\hat{\rho}_k \hat{a}^2} \delta \hat{T}_k \delta(\hat{r} - \hat{r}_k), \quad (C20)$$

$$\hat{r} \frac{\partial \hat{\Delta\Omega}_{\phi k}}{\partial \hat{t}} - \frac{1}{\hat{\tau}_{Mk}} \frac{\partial}{\partial \hat{r}} \left(\hat{r} \frac{\partial \hat{\Delta\Omega}_{\phi k}}{\partial \hat{r}} \right) + \frac{1}{\hat{\tau}_{\phi k}} \hat{r} \hat{\Delta\Omega}_{\phi k} = \frac{n}{2\hat{\rho}_k} \delta \hat{T}_k \delta(\hat{r} - \hat{r}_k) \quad (C21)$$

and

$$\frac{\partial \Delta \hat{\Omega}_{0k}(0, \hat{t})}{\partial \hat{r}} = \frac{\partial \Delta \hat{\Omega}_{\phi k}(0, \hat{t})}{\partial \hat{r}} = 0, \quad (\text{C22})$$

$$\Delta \hat{\Omega}_{0k}(1, \hat{t}) = \Delta \hat{\Omega}_{\phi k}(1, \hat{t}) = 0. \quad (\text{C23})$$

4. Solution of plasma angular equations of motion

Let⁶⁰

$$\Delta \hat{\Omega}_{0k}(\hat{r}, \hat{t}) = -\frac{1}{m_k} \sum_{p=1, P} \alpha_{k,p}(\hat{t}) \frac{y_p(\hat{r})}{y_p(\hat{r}_k)}, \quad (\text{C24})$$

$$\Delta \hat{\Omega}_{\phi k}(\hat{r}, \hat{t}) = \frac{1}{n} \sum_{p=1, P} \beta_{k,p}(\hat{t}) \frac{z_p(\hat{r})}{z_p(\hat{r}_k)}, \quad (\text{C25})$$

where

$$y_p(\hat{r}) = \frac{J_1(j_{1,p} \hat{r})}{\hat{r}}, \quad (\text{C26})$$

$$z_p(\hat{r}) = J_0(j_{0,p} \hat{r}) \quad (\text{C27})$$

and $P \gg 1$. Here, $J_m(z)$ is a standard Bessel function, and $j_{m,p}$ denotes the p th zero of the $J_m(z)$ Bessel function.⁶¹ Note that Eqs. (C24) and (C25) automatically satisfy the boundary conditions Eqs. (C22) and (C23).

It is easily demonstrated that⁶¹

$$\frac{d}{d\hat{r}} \left(\hat{r}^3 \frac{dy_p}{d\hat{r}} \right) = -j_{1,p}^2 \hat{r}^3 y_p, \quad (\text{C28})$$

$$\frac{d}{d\hat{r}} \left(\hat{r} \frac{dz_p}{d\hat{r}} \right) = -j_{0,p}^2 \hat{r} z_p \quad (\text{C29})$$

and⁶²

$$\int_0^1 \hat{r}^3 y_p(\hat{r}) y_q(\hat{r}) d\hat{r} = \frac{1}{2} [J_2(j_{1,p})]^2 \delta_{pq}, \quad (\text{C30})$$

$$\int_0^1 \hat{r} z_p(\hat{r}) z_q(\hat{r}) d\hat{r} = \frac{1}{2} [J_1(j_{0,p})]^2 \delta_{pq}. \quad (\text{C31})$$

Hence, Eqs. (C20) and (C21) yield

$$(1 + 2q_k^2) \frac{d\alpha_{k,p}}{d\hat{t}} + \left(\frac{j_{1,p}^2}{\hat{\tau}_{Mk}} + \frac{1}{\hat{\tau}_{\phi k}} \right) \alpha_{k,p} = \frac{m_k^2 [y_p(\hat{r}_k)]^2}{\hat{\rho}_k \hat{a}^2 [J_2(j_{1,p})]^2} \delta \hat{T}_k, \quad (\text{C32})$$

$$\frac{d\beta_{k,p}}{d\hat{t}} + \left(\frac{j_{0,p}^2}{\hat{\tau}_{Mk}} + \frac{1}{\hat{\tau}_{\phi k}} \right) \beta_{k,p} = \frac{n^2 [z_p(\hat{r}_k)]^2}{\hat{\rho}_k [J_1(j_{0,p})]^2} \delta \hat{T}_k. \quad (\text{C33})$$

It follows that

$$\hat{\Omega}_\theta(\hat{r}_k, \hat{t}) = \hat{\Omega}_{\theta 0}(\hat{r}_k) - \sum_{k'=1, K}^{p=1, P} \frac{\alpha_{k',p}(\hat{t})}{m_{k'}} \frac{y_p(\hat{r}_k)}{y_p(\hat{r}_{k'})}, \quad (\text{C34})$$

$$\hat{\Omega}_\phi(\hat{r}_k, \hat{t}) = \hat{\Omega}_{\phi 0}(\hat{r}_k) + \sum_{k'=1, K}^{p=1, P} \frac{\beta_{k',p}(\hat{t})}{n} \frac{z_p(\hat{r}_k)}{z_p(\hat{r}_{k'})}. \quad (\text{C35})$$

Here, k indexes the various resonant surfaces in the plasma, whereas p indexes the various velocity harmonics.

APPENDIX D: RESONANT PLASMA RESPONSE

1. Rutherford island width evolution equation

The response of the plasma to the RMP in the immediate vicinities of the various resonant surfaces is governed by nonlinear magnetic island physics.³⁰ The amplitude of the reconnected magnetic flux driven at the k th resonant surface is determined by the Rutherford island width evolution equation,^{63,64} which can be written in the form

$$S_k \left(\hat{\Psi}_k^{1/2} + \hat{\delta}_k \right) \frac{d\hat{\Psi}_k}{d\hat{t}} = \sum_{k'=1, K} \hat{E}_{kk'} \hat{\Psi}_{k'} \cos(\varphi_k - \varphi_{k'} - \zeta_{kk'}) + \hat{E}_{kk} \hat{\chi}_k \cos(\varphi_k - \zeta_k), \quad (\text{D1})$$

where

$$S_k = \frac{2\mathcal{I}}{\hat{r}_k \hat{a}} \left(\frac{q}{gs} \right)^{1/2} \frac{\tau_R(\hat{r}_k)}{\tau_A}, \quad (\text{D2})$$

$$s(\hat{r}) = \frac{d \ln q}{d \ln r}, \quad (\text{D3})$$

$$\tau_R(\hat{r}) = \mu_0 r^2 Q_{00}^{ee} \sigma_{ee} \quad (\text{D4})$$

and $\mathcal{I} = 0.8227$. Here, $Q_{00}^{ee}(r)$ is defined in Appendix B, and

$$\sigma_{ee}(r) = \frac{n_e e^2 \tau_{ee}}{m_e}, \quad (\text{D5})$$

where $\tau_{ee}(r)$ is defined in Appendix B. Moreover, $\hat{\delta}_k = \delta_{SC}(\hat{r}_k)/a$, where $\delta_{SC}(\hat{r})$ is the semi-collisional linear layer width specified in Ref. 30. The dimensionless quantity $\hat{\delta}_k$ is merely used to regularize Eq. (D1) so as to prevent it from becoming singular as $\hat{\Psi}_k$ approaches zero. Here, we are neglecting terms in the Rutherford equation which scale as the inverse island width compared to the RMP drive term, which scales as the inverse square of the island width.³⁰

2. No-slip constraint

The helical phase of the reconnected flux driven at the k th resonant surface is determined by the no-slip constraint,³⁴ which can be written in the form

$$\frac{d\varphi_k}{d\hat{t}} = m_k \hat{\Omega}_\theta(\hat{r}_k, \hat{t}) - n \hat{\Omega}_\phi(\hat{r}_k, \hat{t}) \quad (\text{D6})$$

or

$$\frac{d\varphi_k}{d\hat{t}} = \hat{\omega}_{k0} - \sum_{k'=1, K}^{p=1, P} \frac{m_k}{m_{k'}} \frac{y_p(\hat{r}_k)}{y_p(\hat{r}_{k'})} \alpha_{k',p}(\hat{t}) - \sum_{k'=1, mK}^{p=1, P} \frac{z_p(\hat{r}_k)}{z_p(\hat{r}_{k'})} \beta_{k',p}(\hat{t}), \quad (\text{D7})$$

where

$$\hat{\omega}_{k0} = m_k \hat{\Omega}_{\theta 0}(\hat{r}_k) - n \hat{\Omega}_{\phi 0}(\hat{r}_k) \quad (\text{D8})$$

is the (normalized) unperturbed helical phase velocity of the tearing mode resonant at the k th resonant surface, and use has been made of Eqs. (C34) and (C35).

According to the analysis of Ref. 45

$$\hat{\omega}_{k0} = -n \left(\hat{\omega}_E + \left[1 - L_{00}^{ii} + L_{01}^{ii} \left(\frac{\eta_i}{1 + \eta_i} \right) \right] \hat{\omega}_{*i} - \left[L_{00}^{il} - L_{01}^{il} \left(\frac{\eta_l}{1 + \eta_l} \right) \right] \hat{\omega}_{*l} \right), \quad (D9)$$

where

$$\hat{\omega}_E(r) = -\frac{\tau_A}{B_0} \frac{q}{g} \frac{1}{r} \frac{d\Phi}{dr}, \quad (D10)$$

$$\hat{\omega}_{*a}(r) = -\frac{\tau_A}{e_a B_0} \frac{T_a}{g} \frac{q}{r} \frac{d \ln p_a}{dr}, \quad (D11)$$

$$\eta_a(r) = \frac{d \ln T_a}{d \ln n_a}. \quad (D12)$$

Here, $\Phi(r)$ is the electric scalar potential, whereas $p_a(r) = n_a T_a$. The parameters $L_{00}^{ii}(r)$, $L_{01}^{ii}(r)$, $L_{00}^{il}(r)$, and $L_{01}^{il}(r)$ are defined in Appendix B.

APPENDIX E: COMPLETE MODEL

Our complete model can be expressed as the following closed set of equations:

$$S_k \left(|\hat{\Psi}_k|^{1/2} + \hat{\delta}_k \right) \frac{d\hat{\Psi}_k}{dt} = \sum_{k'=1,K} \hat{E}_{kk'} \hat{\Psi}_{k'} \cos(\varphi_k - \varphi_{k'} - \zeta_{kk'}) + \hat{E}_{kk} \hat{\chi}_k \cos(\varphi_k - \zeta_k), \quad (E1)$$

$$\frac{d\varphi_k}{dt} = \hat{\omega}_{k0} - \sum_{k'=1,K}^{p=1,P} \frac{m_k}{m_{k'}} \frac{y_p(\hat{r}_k)}{y_p(\hat{r}_{k'})} \alpha_{k',p} - \sum_{k'=1,K}^{p=1,P} \frac{z_p(\hat{r}_k)}{z_p(\hat{r}_{k'})} \beta_{k',p}, \quad (E2)$$

$$(1 + 2q_k^2) \frac{d\alpha_{k,p}}{dt} + \left(\frac{j_{1,p}^2}{\hat{\tau}_{Mk}} + \frac{1}{\hat{\tau}_{0k}} \right) \alpha_{k,p} = \frac{m_k^2 [y_p(\hat{r}_k)]^2}{\hat{\rho}_k \hat{a}^2 [j_2(j_{1,p})]^2} \delta \hat{T}_k, \quad (E3)$$

$$\frac{d\beta_{k,p}}{dt} + \left(\frac{j_{0,p}^2}{\hat{\tau}_{Mk}} + \frac{1}{\hat{\tau}_{\phi k}} \right) \beta_{k,p} = \frac{n^2 [z_p(\hat{r}_k)]^2}{\hat{\rho}_k [j_1(j_{0,p})]^2} \delta \hat{T}_k, \quad (E4)$$

where

$$\delta \hat{T}_k = \sum_{k' \neq k} \hat{E}_{kk'} \hat{\Psi}_{k'} \hat{\Psi}_k \sin(\varphi_k - \varphi_{k'} - \zeta_{kk'}) + \hat{E}_{kk} \hat{\Psi}_k \hat{\chi}_k \sin(\varphi_k - \zeta_k). \quad (E5)$$

Here, k indexes the resonant surfaces within the plasma, whereas p indexes the velocity harmonics. The full radial width (in r) of the island chain driven at the k th resonant surface is

$$W_k = 4R_0 \left(\frac{q}{gs} \right)^{1/2} |\hat{\Psi}_k|^{1/2}. \quad (E6)$$

Note that we can simplify the numerical solution of Eq. (E1) by extending our definition of $\hat{\Psi}_k$ to allow it to take negative, as well as positive, values. A negative value for $\hat{\Psi}_k$ represents a magnetic island chain at the k th resonant surface whose helical phase is shifted by π radians with respect to one for which $\hat{\Psi}_k$ takes an equal and opposite value.

DATA AVAILABILITY

The data that support the findings of this study are available from the corresponding author upon reasonable request.

REFERENCES

- ¹F. Wagner, G. Becker, K. Behringer, D. Campbell, A. Eberhagen, W. Engelhardt, G. Fussmann, O. Gehre, J. Gernhardt, G. v. Gierke *et al.*, *Phys. Rev. Lett.* **49**, 1408 (1982).
- ²H. Zohm, *Plasma Phys. Controlled Fusion* **38**, 105 (1996).
- ³N. Den Harden, S. Brezinsek, T. Pütterich, N. Fedorczak, G. F. Matthews, A. Meigs, M. F. Stamp, M. C. M. van de Sanden, G. J. Van Rooij, and JET Contributors, *Nucl. Fusion* **56**, 026014 (2016).
- ⁴A. Loarte, G. Saibene, R. Sartori, M. Bécoulet, L. Horton, T. Eich, A. Herrmann, M. Laux, G. Matthews, S. Jachmich *et al.*, *J. Nucl. Mater.* **313–316**, 962 (2003).
- ⁵T. E. Evans, R. A. Moyer, J. G. Watkins, P. R. Thomas, T. H. Osborne, J. A. Boedo, M. E. Fenstermacher, K. H. Finken, R. J. Groebner, M. Groth *et al.*, *Phys. Rev. Lett.* **92**, 235003 (2004).
- ⁶Y. Liang, H. R. Koslowski, P. R. Thomas, E. Nardon, B. Alper, P. Andrew, Y. Andrew, G. Arnoux, Y. Baranov, M. Bécoulet *et al.*, *Phys. Rev. Lett.* **98**, 265004 (2007).
- ⁷W. Suttrop, T. Eich, J. C. Fuchs, S. Günter, A. Janzer, A. Herrmann, A. Kallenbach, P. T. Lang, T. Lunt, M. Maraschek *et al.*, *Phys. Rev. Lett.* **106**, 225004 (2011).
- ⁸Y. M. Jeon, J.-K. Park, S. W. Yoon, W. H. Ko, S. G. Lee, K. D. Lee, G. S. Yun, Y. U. Nam, W. C. Kim, J.-G. Kwak, K. S. Lee, H. K. Kim, H. L. Yang *et al.*, *Phys. Rev. Lett.* **109**, 035004 (2012).
- ⁹A. Kirk, I. T. Chapman, Y. Liu, P. Cahyna, P. Denner, G. Fishpool, C. J. Ham, J. R. Harrison, Y. Liang, E. Nardon, S. Saarelma, R. Scannell, A. J. Thornton, and MAST Team, *Nucl. Fusion* **53**, 043007 (2013).
- ¹⁰T. Sun, Y. Liang, Y. Q. Liu, S. Gu, X. Yang, W. Guo, T. Shi, M. Jia, L. Wang, B. Lyu *et al.*, *Phys. Rev. Lett.* **117**, 115001 (2016).
- ¹¹J. W. Connor, R. J. Hastie, H. R. Wilson, and R. L. Miller, *Phys. Plasmas* **5**, 2687 (1998).
- ¹²M. E. Fenstermacher, T. E. Evans, T. H. Osborne, M. J. Schaffer, M. P. Aldan, J. S. deGrassie, P. Gohil, I. Joseph, R. A. Moyer, P. B. Snyder, R. J. Groebner, M. Jakubowski, A. W. Leonard, O. Schmitz, and DIII-D Team, *Phys. Plasmas* **15**, 056122 (2008).
- ¹³M. Bécoulet, F. Orain, P. Maget, N. Mellet, X. Garbet, E. Nardon, G. T. A. Huijsmans, T. Casper, A. Loarte, P. Cahyna, A. Smolyakov *et al.*, *Nucl. Fusion* **52**, 054003 (2012).
- ¹⁴O. Schmitz, T. E. Evans, M. E. Fenstermacher, M. Lehnen, H. Stoschus, E. A. Unterberg, J. W. Coenen, H. Frerichs, M. W. Jakubowski, R. Laengner *et al.*, *Nucl. Fusion* **52**, 043005 (2012).
- ¹⁵M. J. Lancot, R. J. Buttery, J. S. deGrassie, T. E. Evans, N. M. Ferraro, J. M. Hanson, S. R. Haskey, R. A. Moyer, R. Nazikian, T. H. Osborne *et al.*, *Nucl. Fusion* **53**, 083019 (2013).
- ¹⁶C. Paz-Soldan, R. Nazikian, S. R. Haskey, N. C. Logan, E. J. Strait, N. M. Ferraro, J. M. Hanson, J. D. King, M. J. Lancot, R. A. Moyer *et al.*, *Phys. Rev. Lett.* **114**, 105001 (2015).
- ¹⁷R. Nazikian, C. Paz-Soldan, J. D. Callen, J. S. deGrassie, D. Eldon, T. E. Evans, N. M. Ferraro, B. A. Grierson, R. J. Groebner, S. R. Haskey *et al.*, *Phys. Rev. Lett.* **114**, 105002 (2015).
- ¹⁸C. Paz-Soldan, R. Nazikian, L. Cui, B. C. Lyons, D. M. Orlov, A. Kirk, N. C. Logan, T. H. Osborne, W. Suttrop, and D. B. Weisberg, *Nucl. Fusion* **59**, 056012 (2019).
- ¹⁹Q. Yu, S. Günter, and B. D. Scott, *Phys. Plasmas* **10**, 797 (2003).
- ²⁰Q. Yu, *Nucl. Fusion* **50**, 025014 (2010).
- ²¹Q. Yu and S. Günter, *Nucl. Fusion* **51**, 073030 (2011).
- ²²Q. M. Hu, R. Nazikian, B. A. Grierson, N. C. Logan, J.-K. Park, C. Paz-Soldan, and Q. Yu, *Phys. Plasmas* **26**, 120702 (2019).
- ²³F. Orain, M. Hoelzl, F. Mink, M. Willensdorfer, M. Bécoulet, M. Dunne, S. Günter, G. T. A. Huijsmans, K. Lackner, S. Pamela *et al.*, *Phys. Plasmas* **26**, 042503 (2019).
- ²⁴H. P. Furth, J. Killeen, and M. N. Rosenbluth, *Phys. Fluids* **6**, 459 (1963).

- ²⁵R. Fitzpatrick, R. J. Hastie, T. J. Martin, and C. M. Roach, *Nucl. Fusion* **33**, 1533 (1993).
- ²⁶C. C. Hegna, *Phys. Plasmas* **6**, 3980 (1999).
- ²⁷S. Tokuda, *Nucl. Fusion* **41**, 1037 (2001).
- ²⁸A. H. Glasser, Z. R. Wang, and J.-K. Park, *Phys. Plasmas* **23**, 112506 (2016).
- ²⁹R. Fitzpatrick, *Phys. Plasmas* **24**, 072506 (2017).
- ³⁰R. Fitzpatrick, *Phys. Plasmas* **27**, 042506 (2020).
- ³¹S. R. Haskey, M. J. Lanctot, Y. Q. Liu, C. Paz-Soldan, J. D. King, B. D. Blackwell, and O. Schmitz, *Plasma Phys. Controlled Fusion* **57**, 025015 (2015).
- ³²D. A. Ryan, Y. Q. Liu, A. Kirk, W. Suttrop, B. Dudson, M. Dunne, R. Fischer, J. C. Fuchs, M. Garcia-Munoz, B. Kurzan *et al.*, *Plasma Phys. Controlled Fusion* **57**, 095008 (2015).
- ³³J. K. Park and N. C. Logan, *Phys. Plasmas* **24**, 032505 (2017).
- ³⁴R. Fitzpatrick, *Nucl. Fusion* **33**, 1049 (1993).
- ³⁵O. Sauter, C. Angioni, and Y. R. Lin-Liu, *Phys. Plasmas* **6**, 2834 (1999).
- ³⁶Y. B. Kim, P. H. Diamond, and R. J. Groebner, *Phys. Fluids B* **3**, 2050 (1991).
- ³⁷Y. B. Kim, P. H. Diamond, and R. J. Groebner, *Phys. Fluids B* **4**, 2996 (1992).
- ³⁸S. P. Hirshman and D. J. Sigmar, *Nucl. Fusion* **21**, 1079 (1981).
- ³⁹K.-H. Chung, M. H. Chen, W. L. Morgan, Y. Ralchenko, and R. W. Lee, *High Energy Density Phys.* **1**, 3 (2005).
- ⁴⁰W. L. Rowan, A. G. Meigs, R. L. Hickok, P. M. Schoch, X. Z. Yang, and B. Z. Zhang, *Phys. Fluids B* **4**, 917 (1992).
- ⁴¹P. Monier-Garbet, K. H. Burrell, F. L. Hinton, J. Kim, X. Garbet, and R. J. Groebner, *Nucl. Fusion* **37**, 403 (1997).
- ⁴²R. Andre, *Bull. Am. Phys. Soc.* **57**, 12 (2012).
- ⁴³G. L. Jackson, P. M. Anderson, J. Bialek, W. P. Cary, G. L. Campbell, A. M. Garofalo, R. Hatcher, A. G. Kellman, R. J. LaHaye, A. Nagy *et al.*, in *Proceedings of the 30th EPS Conference on Controlled Fusion and Plasma Physics*, St. Petersburg, Russia (2003), CD-ROM, p. P-4.47.
- ⁴⁴H. Luetjens, A. Bondeson, and O. Sauter, *Comput. Phys. Commun.* **97**, 219 (1996).
- ⁴⁵R. Fitzpatrick, *Phys. Plasmas* **25**, 082513 (2018).
- ⁴⁶C. F. Barnett, *Atomic Data for Fusion* (Oak Ridge National Laboratory, TN, 1990), Vol. 1, p. ORNL-6086.
- ⁴⁷R. J. La Haye, C. C. Petty, E. J. Strait, F. L. Waelbroeck, and H. R. Wilson, *Phys. Plasmas* **10**, 3644 (2003).
- ⁴⁸P. Buratti, E. Alessi, M. Baruzzo, A. Casolari, E. Giovannozzi, C. Giroud, N. Hawkes, S. Menmuir, G. Pucella, and JET Contributors, *Nucl. Fusion* **56**, 076004 (2016).
- ⁴⁹R. J. Hawryluk, *Physics of Plasma Close to Thermonuclear Conditions* (Commission of the European Communities, Brussels, 1980), Vol. 1, Internal Document No. DUR-FU-BRU-XII/476180.
- ⁵⁰R. Fitzpatrick, *Phys. Plasmas* **2**, 825 (1995).
- ⁵¹N. N. Gorelenkov, R. V. Budny, Z. Chang, M. V. Gorelenkova, and L. E. Zakharov, *Phys. Plasmas* **3**, 3379 (1996).
- ⁵²Z. Chang and J. D. Callen, *Nucl. Fusion* **30**, 219 (1990).
- ⁵³I. S. Gradshteyn and I. M. Ryzhik, *Table of Integrals, Series, and Products*, Corrected and Enlarged Edition (Academic Press, New York, 1980), Eq. 8.85.1.
- ⁵⁴A. H. Boozer and C. Nührenberg, *Phys. Plasmas* **13**, 102501 (2006).
- ⁵⁵J. K. Park, M. J. Schaffer, J. E. Menard, and A. H. Boozer, *Phys. Rev. Lett.* **99**, 195003 (2007).
- ⁵⁶S. P. Hirshman, *Nucl. Fusion* **18**, 917 (1978).
- ⁵⁷T. H. Stix, *Phys. Fluids* **16**, 1260 (1973).
- ⁵⁸K. S. Shaing, *Phys. Plasmas* **10**, 1443 (2003).
- ⁵⁹A. J. Cole, C. C. Hegna, and J. D. Callen, *Phys. Plasmas* **15**, 056102 (2008).
- ⁶⁰B. E. Chapman, R. Fitzpatrick, D. Craig, P. Martin, and G. Spizza, *Phys. Plasmas* **11**, 2156 (2004).
- ⁶¹*Handbook of Mathematical Functions with Formulas, Graphs, and Mathematical Tables*, edited by M. Abramowitz and I. A. Stegun (Dover, New York, 1965), Chap. 9.
- ⁶²I. S. Gradshteyn and I. M. Ryzhik, *Table of Integrals, Series, and Products* (Academic Press, New York, 1980), Eq. 6.521.1.
- ⁶³P. H. Rutherford, *Phys. Fluids* **16**, 1903 (1973).
- ⁶⁴P. H. Rutherford, *Basic Physical Processes of Toroidal Fusion Plasmas* (Commission of the European Communities, Brussels, 1985), Vol. 2, p. 531.